University of Stavanger

Faculty of Science and Technology

MASTER'S THESIS

Study program/ Specialization: **Master of Science in Marine and Offshore Technology**	Autumn semester, 2019 **Open** / Restricted access
Writer: **Robel Mussie Amar** **228944**	*Robel Amar* (Writer's signature)
Faculty supervisor: **Dr. Charlotte Obhrai**	
Thesis title: **Estimation of the frequency of breaking waves in deep water from 3D laboratory measurements**	
Credits (ECTS): **30**	
Key words: Wave Tank Experiment Marine Hydrodynamics Breaking Waves Breaking Wave Criteria Continous Wavelet Transform	Pages: 67 + enclosure: 0 Stavanger, 15.12.2019 Date/year

Abstract

Wave breaking is an essential aspect of the sea surface process. Although being an emerging area of research over the last 50 years, the phenomenon remains to be fully understood due to the erratic behavior of breaking waves. This area of research is of particular interest in offshore engineering as marine structures subjected to the impact of such waves may cause considerable damage and fatigue. In this thesis, I have been become familiar with the state of the art of this field and I have applied different methods in order to detect and estimate the frequency of breaking waves. MATLAB has been used to analyze 20 sets of data describing the surface elevations recorded in a wave tank. All 20 realizations are generated with the properties: $H_S = 0.373\ m$, $T_P = 2.75\ s$. After Froude-scaling, the surface elevation data from the wave tank simulates the recordings of deep-water ocean waves. Four different wave breaking criteria have been applied to analyze the surface elevations: the geometric criterion, the dynamic criterion, the dynamic criterion by use of continuous wavelet transform, and limiting local energy density peak by use of continuous wavelet transform. To assess the accuracy and the occurrence of breaking waves, these four criteria have been evaluated by three performance metrics: the detection rate, which is defined as the ratio of confirmed breaking wave events over wave events fulfilling the criterion; the rate of false positives, which is defined as the ratio of non-breaking wave events over wave events fulfilling the criterion; and frequency of wave breaking, which is defined as the ratio of confirmed breaking events over all wave events in the realization. These performance metrics are computed for every single realization and then averaged. This study finds that the dynamic criterion has the best performance with an average detection rate of 89.8 %, corresponding average rate of false positive of 10.2 %, and an average breaking wave frequency of 3.38 %. It is concluded that the geometric criterion should be discarded as it poorly captures the irregular and non-linear properties of the surface elevation, at least when the wave events are defined as zero-up-crossing. The other methods, including the dynamic criterion, are considered to have great potential and can most possibly be further developed to better detect breaking wave events.

Acknowledgements

First of all, I would like to acknowledge my supervisor Associate Professor Charlotte Obhrai for providing me the support and guidance to complete this work. I would also thank my parents and siblings, for providing a great learning environment growing up, and for their continuous encouragement and love. Finally, I also owe a great deal of gratitude to my fellow students for their support and motivation, and not least, for making my five years here at the University of Stavanger a great experience.

List of contents

List of Figures

List of Tables

List of symbols

The following list comprise the symbols used in the *Methodology* and *Results and Discussion* chapters

Latin Symbols

$a(t)$	*Local Characteristic Amplitude*
a_E	*Euler Acceleration*
$A(t)$	*Analytical Envelope*
DR	*Detection Rate*
E_{CWT}	*Energy Density Spectrum*
E_{local}	*Local Energy Density*
f_{cut}	*Cut − off Frequency*
f_{peak}	*Peak Frequency*
g	*Acceleration of Gravity*
IF	*Instantaneous Grequency*
ka	*Steepness Factor*
m_0	*Zeroth Spectral Moment*
m_2	*Second Spectral Moment*
$p(f, t)$	*Wavelet Phase Spectrum*
$p(t)$	*Local Phase*
P	*Probability of Breaking/Breaking Frequency*
$ROFP$	*Rate of False Positives*
u	*Particle Crest Velocity*
v	*Slope of Surface Elevation*

Greek symbols

γ	*Limiting Threshold*
λ	*Factor of Onset of Frequency Limits*
ω	*Angular Frequency*

1 Introduction

Wave breaking is an important aspect of the sea surface process. The phenomenon is present at the surface of the oceans and it plays an important role for oceanographic processes such as the transfer of momentum, mass and heat between the air and sea (Tęgowski, 2004) and energy dissipation in the wave field (Komen *et al.*, 1994). To structural engineers, wave breaking plays another important role: its shock pressure loads on vertical surfaces should be considered when designing marine structures (DNV-RP-C205, 2010). This requires that such waves must be well understood such that ships and offshore structures can be dimensioned to withstand them. Advancing the knowledge in this field may permit structures to be placed further out at sea where the sea is rougher. The application of this knowledge permits a secure construction of wind farms far out at sea where the winds are stronger, exposed fish farms, deep-sea autonomous ships or the development of oil and gas sites where the remaining reservoirs potentially are larger. Thus, for current and future marine technology, as well as meteorology, understanding the onset of wave breaking and its occurrence is significant.

Yet, wave breaking remains to be fully understood. Due to its complex and erratic nature, determining a definitive set of parameters such that one can expect wave breaking is still challenging. Different approaches to determine the incipience of wave breaking have been employed. These approaches include both theoretical and experimental methods, some of which are: field observation of white caps (Donelan *et al.*, 1972; Holthuijsen & Herbers, 1986), data acquisition and analysis from fields (Ochi & Tsai, 1983), wave tank experiments (Tęgowski, 2004; Banner & Pierson 2007) and numerical simulation of breaking waves (Song & Banner 2002). The waves are also measured on different conditions such as mid-ocean wave breaking, wave breaking due to shoaling, monochromatic waves, and non-linear, 2D waves, 3D waves, different numerical models to simulate waves and wind-forced waves. Additionally, the parameter itself, i.e. the wave breaking criterion, has varied. A wave has several properties and determining which one(s) that indicate(s) breaking is the essence of this study. Alexander Babanin, a professor of Ocean Engineering at the University of Melbourne, has contributed extensively to this field. In 2011, he published a book named *Breaking and Dissipation of Ocean Surface Waves* where he presented the state of art of wave breaking research. Another extensive work on breaking wave research is elaborated by Stanisław R. Massel in *Ocean Waves Breaking and Marine Aerosol Fluxes* (2007).

The objective of this thesis is to perform a literature study and familiarize with the most common breaking wave criteria and methods to detect the occurrence of wave breaking.

Experimental data in the form of point measurements is received from a 3D model test at MARINTEK. By using MATLAB, the different wave breaking criteria will be applied to investigate their accuracy and estimate the frequency of wave breaking. The criteria will be tested for 20 different sets of data of the same sea states. Finally, this thesis will conclude with a recommendation for further work.

2 Theory

Wave breaking occurs when momentarily high crests reach an unstable position (Ochi & Tsai, 1983). *Descriptive Physical Oceanography: An introduction* (Talley *et al.*, 2011) classifies breaking waves at coastal regions into three categories: spilling breakers, plunging breakers, and surging breakers (see *Figure 2-1*). However, wave breaking occurs at deep waters as well. Spilling is characterized by a small spilling turnover at the crest of the wave and it occurs at terrains with low slope. Wave breaking by spilling is significantly affected by surface tension, viscosity and turbulence (Irisov &Voronovic, 2010). Plunging breakers occur on steep slopes and sudden depth changes. The crest curls over and forms a plunging jet and drops into the trough with great impact. Surging breakers are characterized by smooth waves small amount of white capping. According to Talley *et al.*, surging breakers occurs on such steep beaches that "the waves reaches the beach before it has a chance to break".
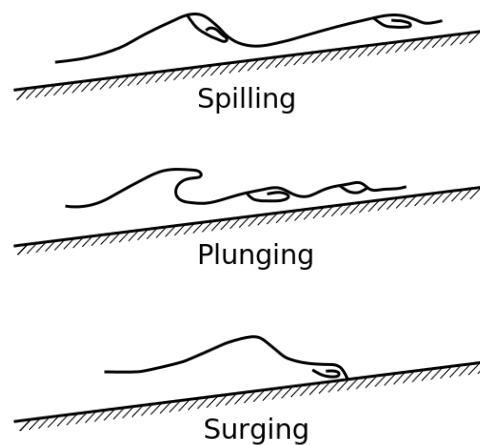
Figure 2-1: Different types of wave breaking

In the literature, researchers generally divide the breaking wave criteria into three main categories: *the geometric criteria*, *the kinematic criteria* and *the dynamic criteria* (Wu & Nepf, 2002). The geometric criteria are based on local wave shape (Kjeldsen & Myrhaug, 1980), and global wave steepness (Rapp & Melville, 1990). The kinematic criteria are based on the difference between the horizontal wave crest particle velocity and phase velocity of the wave group (Longuet-Higgins, 1969). The dynamic criteria is based on acceleration of the wave crest (Longuet-Higgins, 1985), the momentum and energy growth rate (Banner & Tian, 1998), and higher harmonic energy evolution (Rapp & Melville, 1990; Kway *et al.*, 1998). This chapter elaborates on each of these criteria.

2.1 Wave Breaking Measurements

Huge advancements have been made in the field of breaking wave detection in the second half of the 20th century. Traditionally, visual inspection of the sea surface has been the foremost method to detecting wave breaking as per Holthuijsen and Herbers (1986), Babanin (1995), Banner *et al.* (2000) to mention a few. Although visual inspection remains today is the most accurate way to determine whether a wave breaks or not, the method still subjected to human error. Additionally, the method is certainly tedious: it is manually intensive, and it is very ineffective when inspecting a large number of waves.

Many studies involve a mathematical model, ranging from a simple formula to complex functions and integrals, a wave measuring device, and visual inspections of white capping of sea surface to confirm the onset of breaking. Longuet-Higgins and Smith (1983) performed a study with a so-called physical-limiter criterion. Their study hypothesized that a breaking wave is equivalent to a sudden jump of the crest such that if a sensor detects a wave that breaks, the signal will display a steep fall in the surface elevation. They formulated the following:

$$\text{R} = \frac{\Delta\eta}{\Delta t} = c\,\frac{\Delta\eta}{\Delta x} = c\,tan\,\theta \qquad\qquad \textit{Eq. 2-1}$$

Where *η* is surface elevation, *t* is time, *c* is the phase speed, *x* is horizontal displacement, and *θ* is the angle between the horizontal axis and the water surface. They believed that a certain value of R would indicate the onset of breaking. Later, it was reasoned that there is no fixed value of R, nor angle, to determine the onset of breaking. However, it could indicate an in-process wave breaking (Babanin *et al.*, 2007. 2009, 2010).

Tęgowski (2004) performed an experimental study where he investigated different breaking criteria. With data retrieved from the Ocean Basin Laboratory at MARINTEK, Trondheim, paired with video recordings, he investigated wave breaking with respect to the steepness factor *ka*, the fourth spectral moment and wavelet analysis among other methods. Of all the methods he applied, he recommended using the derivative of the surface displacement as per Eq. 2-1. He developed it further by inspecting for wave breaking by using the second derivative of the surface elevation:

$$\frac{d^2\eta}{dt^2} = c\,\frac{ds}{dt} \qquad\qquad \textit{Eq. 2-2}$$

4

Where *s* is the local slope found by differentiating the surface elevation with respect to the horizontal displacement *x*.

A wide range of instruments have been applied to detect wave breaking. Some of which are accelerometers, pressure sensors, acoustic sensors and lasers. Lowen and Melville (1991), Ding and Farmer (1994) and (Babanin A. V., 2001) *et al.* (2001) applied acoustic sensors; Jessup *et al.* (1997) invented an optical method where infrared imaging mapped the position of the surface layer of a breaking wave; Gemmrich and Farmer (1999) inspected for void fraction; Smith *et al.* (1996) and Phillips *et al* (2001) used a high range resolution radar to detect the speed distribution properties of breaking waves.

The reliability of such methods and instruments has increasingly been improved over the years. However, developing, maintaining and installing such equipment are costly, especially if such equipment is placed far out at sea in rough conditions. Therefore, the study of breaking waves has gradually become more theoretical, and in some studies, statistical, in combination with wave tank experiments (Tęgowski, 2004; Banner & Pierson, 2007) and numerical simulations (Song & Banner, 2002; Irisov & Voronovic, 2010). Though, field data will never be irrelevant is it represents the real values on which one wants to investigate the breaking wave criteria. Examples of this are wavelet analysis performed by Torrence and Compo (1998) who use sea surface temperature, and Lui and Babanin (2004) who have studied surface elevation data from Lake George and the Black Sea.

2.2   The Geometric Criteria

In 1880, George Stokes theorizes that a regular, stationary progressive wave will become unstable and unable to sustain its shape if the particle velocity at the wave crest exceeds the phase velocity (Toffoli *et al.*, 2010). In equivalent geometric terms, he finds that the wave crest must be contained within an angle of 120 °. In 1893, Michell derives that, for deep water, the wave height, *H*, should be 0.142 times the wavelength *L'* (Ochi & Tsai, 1983) such that:

$$\text{H} \geq 0.142 \, \text{L}',$$

<div align="right">*Eq. 2-3*</div>

$$\text{L}' = \frac{1.2g}{2\pi f^2}$$

<div align="right">*Eq. 2-4*</div>

Where *L'* is known as Stokes' limiting wavelength, *g* is the acceleration of gravity and *f* is the wave frequency. The height-wavelength relationship is illustrated in Figure 2-2. This theory suggests that the wavelength is proximately 7 unit lengths longer than the wave height. This simplifies the criterion to:

$$\frac{H}{L} \geq \frac{1}{7}$$

Eq. 2-5

However, the most referred geometric criterion stems from inserting Eq. 2-4 into Eq. 2-3 which yields:

$$H \geq 0.027gT^2$$

Eq. 2-6

Eq. 2-4 states that the onset of breaking occurs when the wave height is equal or greater than 0.027 times the product of acceleration of gravity times and the period squared. This criterion has been tried experimentally with results as shown in Table 1 (Massel, 2007). The results express the mean value of the steepness of the several breaking waves, segregated by breaker type. The results are consistently lower than the theoretical limit, and it seems like that plunging breakers occur at marginally higher steepnesses than for spilling breakers.

Table 1: Historical values of Stokes' limiting steepness

		Breaker type	
Researcher(s)		**Plunging**	**Spilling**
Ochi and Tsai	1983	0.020	-
Ramberg and Griffin	1987	-	0.021
Bonmarin	1987	0.022	0.021
Rapp and Melville	1990	0.020	0.020
Griffin *et al*.	1996	0.018 – 0.021	0.017 – 0.018
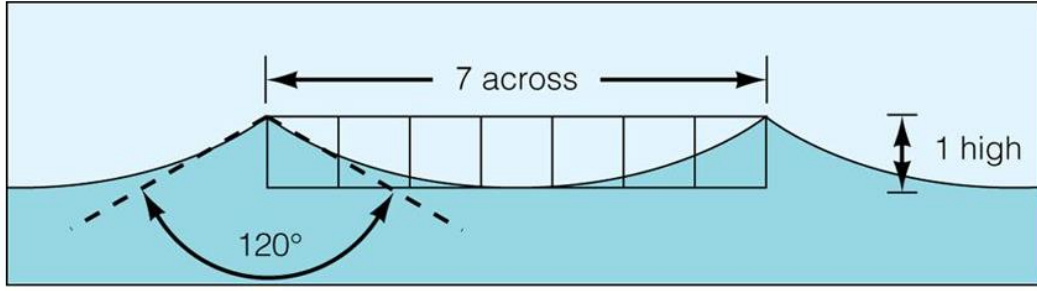
Figure 2-2: Height-wavelength relationship of wave crest within angle of 120 º

Thus, in general terms, one can rewrite Stokes' limiting criterion as:

$$\frac{H}{gT^2} \geq \alpha$$

<div align="right">*Eq. 2-7*</div>

Where α is a dimensionless coefficient which is determined from experiments. Stokes' limiting steepness is commonly rewritten as the steepness factor, ka, which is the product of the wave amplitude, a, and the wavenumber k. From Eq. 2-10, the steepness factor is found by assuming linearity, expressing the period by the angular frequency, and using the dispersion relation assuming deep water:

$$H \frac{1}{T^2} \frac{1}{g} \geq \alpha$$

$$2a\, f^2 \frac{1}{g} \geq \alpha$$

$$2a \left(\frac{\omega}{2\pi}\right)^2 \frac{1}{g} \geq \alpha$$

$$2a \frac{\omega^2}{g} \frac{1}{(2\pi)^2} \geq \alpha$$

$$ka \geq 2\pi^2 \alpha$$

<div align="right">*Eq. 2-8*</div>

From *Eq. 2-8*, the equivalent steepness factors from Table 1, by approximating to two decimals, are *ka ≥ 0.40* (Ochi and Tsai), *ka ≥ 0.41* (Ramberg and Griffin), *ka ≥ {0.43, 0.41}* (Bonmarin), *ka ≥ 0.40* (Rapp and Melville), *ka ≥ {0.36 – 0.41, 0.34 – 0.36}* (Griffin *et al.*). Michell's wave height-wavelength relationship from 1893, expressed as in Eq. 2-5, has the steepness factor of *ka ≥ π/7 ≈ 0.45*. Brown and Jensen (2001) finds that breaking onset occurs at *ka ≥ 0.44* for linearly dispersive focusing of waves. In *Maximum steepness of oceanic waves:*

Field and laboratory experiments (Toffoli *et al*, 2010), four different sets of wave data are collected, two of which are wave tank experiments, and the other two are field observations. All data are produced under different sea states, but they show consistent results: there is an indication that there exists a well-defined value of the wave steepness in which its exceedance the wave will no longer sustain its shape. At an increasingly higher steepness, the waves become vertically asymmetric, and the front-face steepness threshold is found to be 0.55, while the rear-face steepness threshold is found to be slightly above 0.44.

Although the work of Toffoli *et al*. calculates *ka* by taking half the wave height as the amplitude, the strength of applying the steepness factor over Stokes' limiting steepness is that the steepness factor accounts for the horizontal asymmetry of nonlinear waves, i.e. the steepening of wave crests and flattening of wave troughs. However, both these criteria apply global properties of wave events, namely the wave height, wave amplitude, wavenumber and wave period. These global properties poorly describe the distinct features of highly nonlinear ocean waves, such as the complex surface of the individual wave surfaces. Therefore, applying these global properties to identify the slope of breaking events may be overly generalizing and inaccurate.

Myrhaug and Kjeldsen (1978) have developed several parameters to better capture the asymmetrical nature of irregular waves. At first, they separate the different wave events by their down-crossing period, as they argue that the trough being in front of the crest tends to show characteristics relevant to the lagging crest. A down-crossing wave event (moving right to left) with decomposed wave properties is depicted in Figure 2-3. *MWL* represents the mean water line, $\zeta(x)$ denotes the surface elevation, *L*, *T* and *h* denote the global wavelength, wave period and wave height respectively.
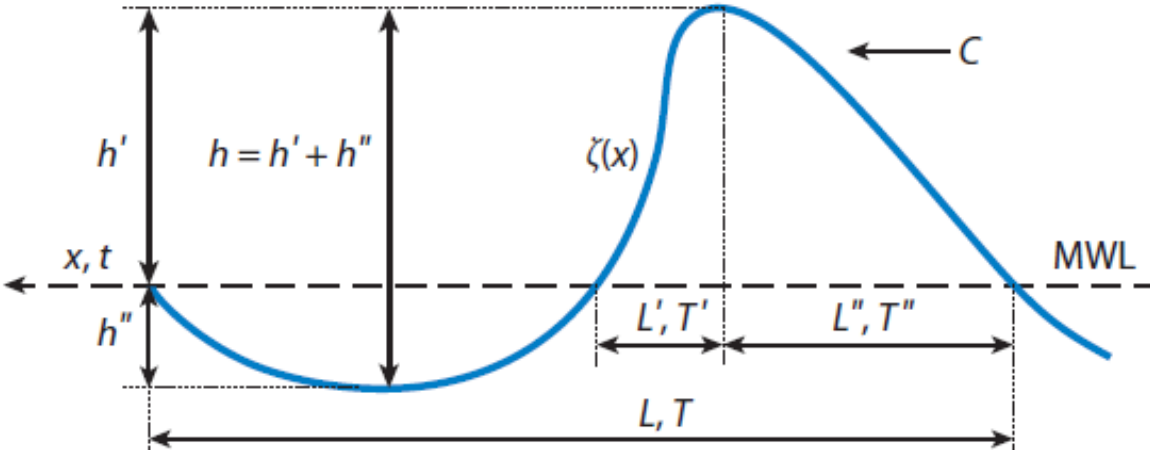
Figure 2-3: Parameterization of asymmetric down-crossing wave event

From the components of the global wave properties, Myrhaug and Kjeldsen define four parameters: the vertical and horizontal asymmetry parameters, the crest-front steepness and the crest-rear steepness. Respectively, these parameters are expressed as:

$$\mu = \frac{h'}{h}$$

$$\beta = \frac{L''}{L'}$$

$$\varepsilon = \frac{h'}{L'} = \frac{2\pi h'}{gTT'}$$

$$\delta = \frac{h'}{L''} = \frac{2\pi h'}{gTT''}$$

Eq. 2-9

Table 2 displays the obtained values for the different parameters mentioned by Perlin *et al.* (2013) and Massel (2007). The steepness is calculated from surface elevation in time domain with the exception from Bonmarin. Certain experiments are conducted with 3D waves, where the steepness is explored relative to wave focusing, spreading, and to convergence into a 2D wave.

Table 2: Historical values of crest-front steepness and asymmetry parameters

Researcher(s)		ε	β	μ
Sinusoidal wave		2 H/L	1/2	1
Stokes 2nd order wave		0.4	1	0.61
Kjeldsen and Myrhaug	1986	0.32 – 0.78	0.9	2.0
Bonmarin*	1989	0.38 – 0.61	1.2 – 2.4	0.60 – 0.77
She *et al.***	1994	0.51 – 1.02	0.65 – 0.67	-
Nepf *et al.***	1998	0.32 – 0 .56	-	-
Wu and Nepf**	2002	0.39 – 0.41	-	-

* Calculated from spatial definition

** Calculated from of 3D waves

Although this method considers more local properties of highly asymmetric waves, its universality is less than of the steepness factor as it is sensitive to the type of experiment being

performed. Also, the steepnesses are defined both in time domain and space domain, but there is no straightforward method to transform the surface elevation between the two different domains. This means that the two different methods do not calculate the same characteristic, and that when calculating the steepnesses in time domain, it will not necessarily reflect the height-wavelength components ratio as given in Figure 2-3.

2.3   The Kinematic Criteria

The kinematic criterion suggests that if the horizontal fluid particle in a wave crest exceeds the phase velocity, the wave will break. If u denotes the particle velocity and c denotes the phase speed, one can express the kinematic criterion as the following:

$$u \geq c$$

Or more conventionally,

$$\frac{u}{c} \geq 1$$

Eq. 2-10

The disadvantage of the kinematic criterion is its difficulty to accurately determine the phase and particle velocity of irregular waves, especially from experimental data. Banner and Peregrine (1993) state that due to the unstable form of the wave crest, there is no given crest velocity, but rather a range of velocities that correspond the "true" crest velocity. Gemmrich (2005) underline that indirect methods to calculate these velocities are invalid of rotational waves.

Stansell and MacFarlane (2002) use three different definitions to express Eq. 2-10 to assess the validity of the kinematic criterion. Firstly, the wave was considered as a linear wave, meaning the period and wavelength of the non-linear wave were taken as constant. The second definition is based on partial Hilbert transform of the surface elevation data with instantaneous values for space and time. The third definition is based on direct measurement of the speed at the surface elevation maximum. It is found that the linear assumption yields a poor estimate of the "true" velocities compared to the second and third definition that apply local properties of the wave. The study finds the highest ratios to be *0.81* for plunging breakers and *0.95* for spilling breakers, concluding that the criteria is invalid. It is suggested that this criterion can be

considered as the ultimate limit for a wave to sustain itself rather than the condition for the onset of breaking.

Massel (2007) elaborates on how to estimate the local crest and phase velocities from a wave record. Beginning with a definition of the phase speed for a linear regular wave:

$$c = \frac{\omega}{k}$$

The wavenumber k is typically estimated from the spatial property of the surface elevation (Stansell & MacFarlane, 2002), which is unavailable in wave records captured in time domain. By using the dispersion relation in deep water, the phase velocity is now defined as:

$$c = \frac{\omega}{\left(\frac{\omega^2}{g}\right)}$$

$$c = \frac{g}{\omega} \qquad\qquad \textit{Eq. 2-11}$$

However, this calculation of phase speed is only valid for linear waves still. The analytical surface elevation, as well as the instantaneous crest and phase velocities, are obtained by the so-called phase-time method (PTM) based on the Hilbert transform. Having that the surface elevation is denoted ζ *(t)*, its Hilbert transform ξ *(t)*, the analytical signal, η *(t)*, is then expressed as:

$$\eta(t) = \zeta(t) + i\,\xi(t)$$

Where components are expressed by:

$$\zeta(t) = \sum_{n=0}^{\infty} [a_n \cos(n\omega t) + b_n \sin(n\omega t)]$$

$$\xi(t) = \sum_{n=0}^{\infty} [a_n \sin(n\omega t) - b_n \cos(n\omega t)]$$

The surface elevation is leading with a phase of $\pi/2$. Therefore, the Hilbert transform can be regarded as the horizontal component of the surface elevation. The instantaneous horizontal velocity, *u (t)*, at the free surface becomes:

$$u(t) = \frac{\partial \xi(t)}{\partial t}$$

In Euler form, the analytical signal is expressed as:

$$\eta(t) = A(t)e^{i\theta(t)}$$

Where

$$A(t) = \sqrt{\zeta(t)^2 + \xi(t)^2}$$

$$\theta(t) = \arctan\left(\frac{\xi(t)}{\zeta(t)}\right)$$

The instantaneous angular frequency is then found by differentiating the argument:

$$\omega(t) = \frac{\partial \theta(t)}{\partial t}$$

Thus, the kinematic criterion is rewritten by substituting Eq. 2-11, Eq. 2-12, and Eq. 2-13 into Eq. 2-10:

$$\frac{u}{c} \geq 1$$

$$u(t) \cdot \frac{1}{\left(\frac{g}{\omega(t)}\right)} \geq 1$$

$$u(t) \frac{\omega(t)}{g} \geq 1$$

$$\frac{\partial \xi(t)}{\partial t} \frac{\partial \theta(t)}{\partial t} \frac{1}{g} \geq 1$$

2.4 The Dynamic Criteria

The classic dynamic criterion concerns the downward acceleration of the wave crest particle relative to the acceleration of gravity (Wu & Nepf, 2002). Having the surface elevation is expressed as a linear wave:

$$\eta(x,t) = a \sin(\omega t - kx)$$

The acceleration at the wave surface is obtained by taking the second time derivative:

$$\frac{\partial^2 \eta(x,t)}{\partial t^2} = -a\omega^2 \sin(\omega t - kx)$$

Thus, the acceleration at the wave crest can be takes as the product of the wave amplitude and the angular frequency. The very same expression is obtained by applying Airy wave theory and deriving the vertical orbital acceleration from the velocity potential at the free surface assuming deep water. With deep water assumption, the velocity potential of a wave particle can be described as the following:

$$\Phi(x,z,t) = \frac{ag}{\omega} e^{kz} \cos(\omega t - kx)$$

Where Φ is the velocity potential, a is the wave crest amplitude, g is the acceleration of gravity, ω is the angular frequency and k the wavenumber. Differentiating with respect to the vertical position z, and time t, the vertical particle acceleration is obtained:

$$\dot{w}(x,z,t) = \frac{\partial \Phi(\mathrm{x,z,t})}{\partial z\, \partial t} = -agk\, e^{kz} \sin(\omega t - kx)$$

At the free surface, and inserting for the dispersion relation, the orbital of the vertical acceleration component becomes:

$$\dot{w}(x,z,t) = -a\omega^2 \sin(\omega t - kx) \qquad\qquad \textit{Eq. 2-15}$$

The surface elevation and the acceleration are in phase, but they are of opposite signs. Figure 2-4 illustrates that the highest downward acceleration occurs at the wave crest.
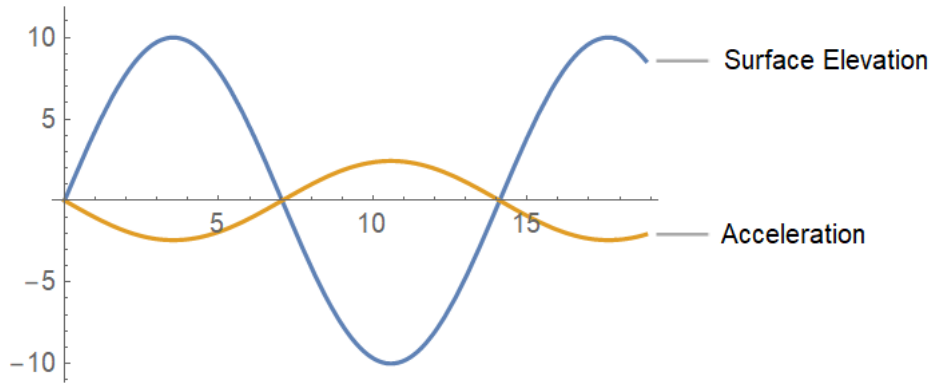

Figure 2-4: Vertical acceleration relative to surface elevation

In field measurements, the acceleration can be directly measured by buoys or accelerometers, and the dynamic criterion takes the form as in Eq. 2-21:

$$a = \gamma g \qquad \text{Eq. 2-16}$$

Where γ is the limiting threshold to be determined empirically. In early studies, several authors suggested different limiting thresholds for this value. Certain examples are $\gamma = -1$ at the free surface (Phillips, 1958), $\gamma = -1/2$ for a 120 º Stokes corner flow (Snyder & Kennedy, 1983), and $\gamma = -0.4$ (Strokosz, 1986). Longuet-Higgins (1985) has an analytical approach to determine the "real" and "apparent" accelerations at the wave crest relative to an increasing steepness factor. The subjected waves are progressive, irrational, symmetric gravity waves at finite depth. The waves are measured by a wave gauge and a free-floating buoy, obtaining two data sets. From the wave gauge, the apparent acceleration is calculated as the Euler acceleration i.e. the double derivate of the surface elevation with respect to time, η_{tt}. With a change of variables, it is calculated as:

$$a_E = c\, \eta_{xx}$$

Where c is the phase speed and η_{xx} is the double partial derivative of the surface elevation in space domain. The real acceleration, measured by the buoy, is Lagrangian and is calculated as:

$$a_L = \boldsymbol{u} \cdot \nabla \boldsymbol{u}$$

Where $\boldsymbol{u} = (u, v)$ is the velocity vector described by the two orbital velocity components. Some of his results are presented in Table 2-3 (Longuet-Higgins, 1985). The table shows the minimum (downward) acceleration computed by the different methods, normalized by the acceleration of gravity for an increasing steepness factor. The apparent Euler acceleration at high steepnesses is found to be unlimited. There might be several reasons for this. In general, when computing the numerical differentiation of field data, the noise of the record distorts the results. The contribution of the noise becomes more prominent at higher order derivatives meaning that the calculated Euler acceleration is exceedingly sensitive to noise. The table shows only abnormally high Euler acceleration at the highest steepness and the explanation for that may be the following: the wave gauge measuring the surface elevation is sensitive to all detection, thus phenomena such as highly irregular small ripples riding on top of the wave crests, aeration of water at the wave surface, or jumping water particles, yield measurements that do not represent the orbital particle position of the wave crest (Massel, 2007). Taking the double derivative of such measurement will give no indication of the downward acceleration at the crest. However, as such phenomena is associated with wave breaking, the detection of extremely high Euler accelerations may be a good indicator of breaking events.

Table 2-3: Steepness factor and acceleration at crest (Longuet-Higgins, 1985)

ak	a_E/g	a_L/g
0.1	-0.1251	-0.0991
0.2	-0.3357	-0.1931
0.3	-0.7795	-0.2784
0.35	-1.2814	-0.3175
0.40	-2.6753	-0.3548
0.4432	- ∞	-0.388

Comparing Table 2-3 to chapter *2.2 The Geometric Criteria* and looking at the values for the steepness, one finds that the critical steepness lies between $ka \geq 0.41$ and $ka \geq 0.44$. This yields real accelerations between $a_L = 0.355\ g$ and $a_L = 0.388\ g$.

For comparison, a wavelet analysis by Liu and Babanin (2004) gained experimental data from the Black Sea measured with an accelerometer. The data is presented as a histogram

plotting the number of waves versus the acceleration divided the acceleration of gravity when the waves are breaking. The highest ratio of acceleration for a continuous distribution with statistical reliability was found to be *a ≈ 0.30 g*.

Based on *On the local properties of highly nonlinear unsteady gravity water waves. Part 2. Dynamics and onset of breaking* (Barthelemy *et al.*, 2015) the same group of researchers published *On a unified breaking onset threshold for gravity waves in deep and intermediate depth water* (2018) where they introduced a new subset of the dynamic criterion which is based on the strength of the local energy flux relative to the local energy density. They suggest that wave breaking may be the waveform's inability to accommodate a certain limit of the local wave energy flux. When this limit is met or exceeded, the wave will overturn. This theory is supported by the visual observation that wave breaking occurs typically at the crest of the tallest dominant wave of a wave group. Starting from the expression of mechanical energy (sum of potential and kinetic energy), the article introduces assumptions and conditions such that a dimensionless parameter B_x expressing the ratio of energy flux and local energy density at the free surface is expressed as:

$$B_x = \frac{U_s}{C} > \text{threshold} \qquad \text{Eq. 2-17}$$

Where U_s is the surface water particle velocity and *C* is the wave crest velocity. This energy flux ratio criterion differs from the kinematic condition where the latter states that the ratios of velocities shall be greater than unity. The energy flux condition does not promote a predetermined value which guarantee breaking when exceeding a threshold value. For their experiment, the onset of breaking occurred when B_x was in the range [*0.85, 0.86*]. Thus, this study concluded with that breaking strictly occurs in advance of the kinematic criterion. The experiment was a numerical study of 2D and 3D waves for intermediate and deep water with flat bottom topography.

Motivated by the work of Barthelemy *et al.* (2015), Saket *et al.* (2015) inspected the condition for marginal breaking and recurrence by investigating a threshold defined the energy flux ratio, which is expressed by Eq. 2-17. The study was conducted in a laboratory with freely propagating, unsteady deep-water waves. The velocities determined by Thermal Image Velocimetry and the energy flux ratio was determined to be in the range of $B_x = 0.840 \pm 0.016$. This result is in good agreement with the result from the numerical study of Barthelemy *et al*. Saket *et al*. concluded also with that their result is robust for waves with different steepnesses.

Seiffert *et al.* (2017) did a numerical study and experimental study breaking waves. For the numerical section of the study, they used a non-linear potential flow solver HOS-NWT. The instantaneous local phase velocity was calculated at every point and for every time step by Hilbert transform and the dispersion relation. The crest velocity was predicted from the phase velocity. This estimation turned out the yield good results when compared to the experimental approach. Breaking was detected by simple video recording and calculations. The ratio was found to be *0.85*. This study concluded also with that this criterion is robust for different types and strengths of breakers.

2.5 Wavelet Transform: An Introduction

A Fourier transform, such as the FFT-algorithm, decomposes any signal into a sum of its constituent trigonometric functions. The characteristic energy or power density spectra give a general description of the entire signal, i.e. the signal's power/energy versus its frequency. Figure 2-5 illustrates such a transform. The signal in time domain is seen in red and is discretized into its three basic trigonometric functions described by their amplitudes and frequencies. From this information one can create a new plot of the signal's energy associated with its respective frequency. Considering field measurements of long-crested irregular sea, the surface elevation can be considered as the sum of a large number of regular wave components, as graphically represented by Figure 2-6. The wave components are ordered after increasing frequency and their corresponding half amplitude squared gives a spectrum of energy density. By fitting the Fourier transform to an ocean-wave spectrum, such as JONSWAP, the energy density spectrum continuous and smooth.
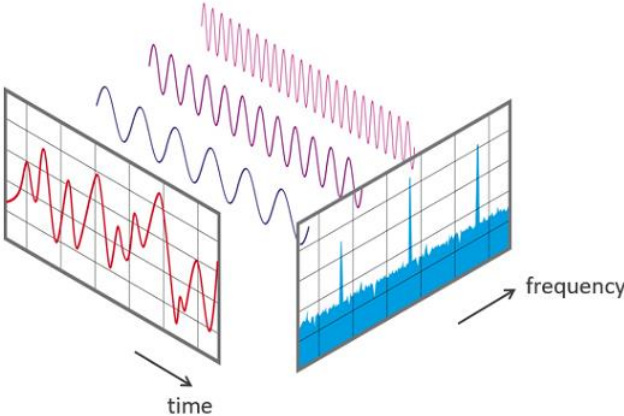

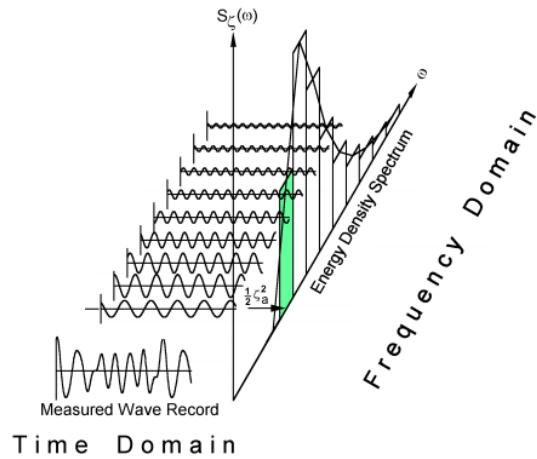*Figure 2-5: FFT of simple time signal*

*Figure 2-6: Energy density spectrum from wave record*

The energy density spectrum as shown in Figure 2-6, has many applications. Some of which are calculating moments, response spectrum of floating structures, and relevant statistical properties of the sea state. However, this spectrum does not provide any temporal location of the energy density. As rapid changes in the localized energy density of the surface process may be linked to wave breaking (Liu & Babanin, 2004), temporal information on the energy density may give a great indication of the occurrence of wave breaking.

To produce the energy spectral density information as a function of time *and* frequency, one could use a windowed Fourier transform as the Short-Time Fourier Transform (STFT). This type of transform sections the signal into time windows of equal length and analyzes these windows sequentially and is thus able to locate the different frequencies into these windows of time. The smaller the time window, the more precise information of the temporal location of the frequency retrieved. However, the size of the time window is also the limit of the maximum period the transform is able to analyze. This means that increasingly smaller time windows exclude lower and lower frequency components of the signal. Thus, the challenge of STFT is to select the appropriate size of the time window to extract relevant information.

The *continuous wavelet transform* (CWT) is a method of signal processing in which a one-dimensional time varying signal is transformed into a two-dimensional function of time and frequency, similar to the STFT. Where the energy density spectrum from the FFT does not consider the temporal localization of the variations within a time series, and assume stationarity of the data, wavelet transform permits non-stationarity and provides information at localized time-frequency domain (Lui, 1993). The STFT assumes stationarity as well, but the STFT can

provide time-frequency information of the signal. The advantage of CWT is that it provides a method to rapidly detect abrupt changes in the signal well localized in both time and frequency.

Figure 2-7 illustrates the working principles of the STFT and CWT as well as the strength of CWT over the STFT. Figure 2-7 a) is a schematic representation of the windowed Fourier transform where the tiles represent the size of the time window. In Figure 2-7 b), a signal consisting of two superimposed hyperbolic chirps are transformed by STFT with a fixed resolution of 50 milliseconds. The two dotted lines represent the instantaneous time and frequency of each of the chirps. As one can see from the scalogram, the components are well localized in time, but inaccurately localized in frequency as well as poorly distinguished from one another. Figure 2-7 c) shows the tiling of the CWT. The wavelet transform can widen its window for low frequencies and narrow it for lower frequencies. The variation of window size permits the localization of both components accurately in both time and frequency. Due to ocean waves consisting of a large number of regular waves, with a wide span in frequencies, the CWT is to prefer over the STFT to interpret the intermittent nature of ocean waves by capturing their temporally localized wave properties such as frequencies and amplitudes (Chen & Chu, 2017).
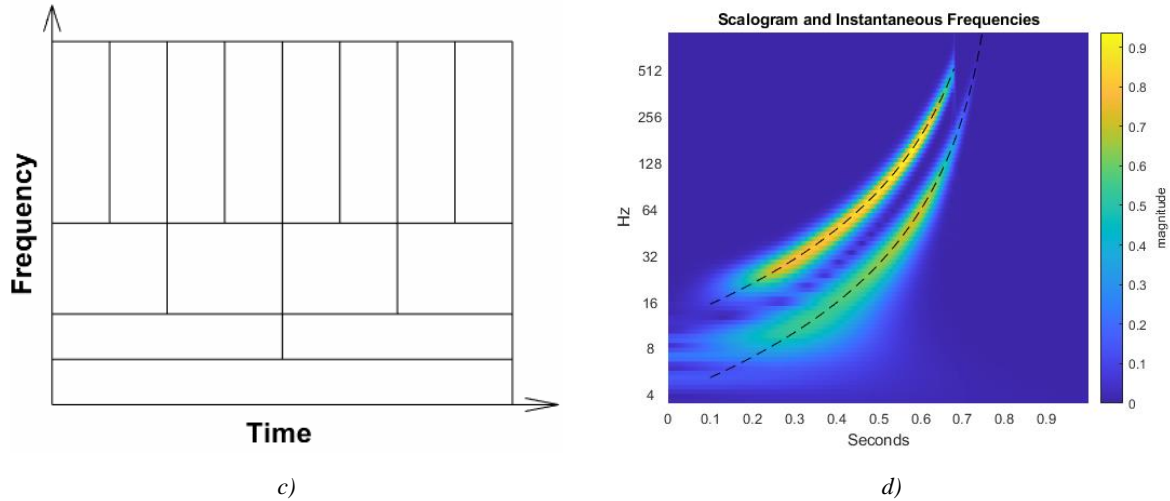

a) *b)*

c)   *d)*
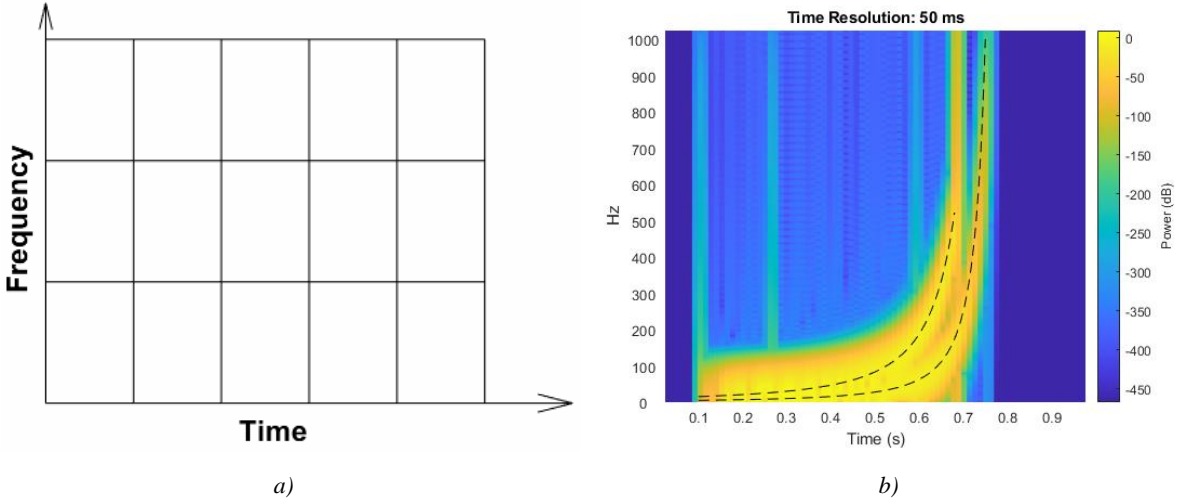
Figure 2-7: A comparison of the STFT to the CWT

The transform is done by scaling the window of analysis and shifting it continuously along the time signal. A given scale of the window shifts through the entire signal and is subsequently increased iteratively for higher scales. The scale corresponds to the stretch of the analyzing wavelet and is thus equivalent to wave frequency. The window of analysis, i.e. the analyzing wavelet, is commonly known as the *mother wavelet*. Mathematically, one can generally express the transform function of a CWT as (Chen & Chu, 2017):

$$W_{X\psi}(s,t) = \int_{-\infty}^{\infty} \frac{1}{\sqrt{s}} \, \psi^* \left(\frac{t'-t}{s} \right) X(t') \, dt'$$

Eq. 2-18

Where $W_{X\psi}$ *(s, t)* is the wavelet transform function, *s* is the scaling factor, *t* is the time shift, ψ^* is the complex conjugate of the mother wavelet and *X (t')* is the surface elevation data. The suitable mother wavelet is determined by what type of signal being analyzed where the shape of the wavelet tries to mimic the shape of the signal. One of the most commonly used wavelets are the Meyer wavelet, Morlet wavelet and Mexican hat wavelet as depicted respectively in *Figure 2-8*, *Figure 2-9* and *Figure 2-10*. There exist many different mother wavelets suited for different applications and one can further develop this list of mother wavelets if one wants to analyze a very particular signal, e.g. Liberzon *et al.* (2019).
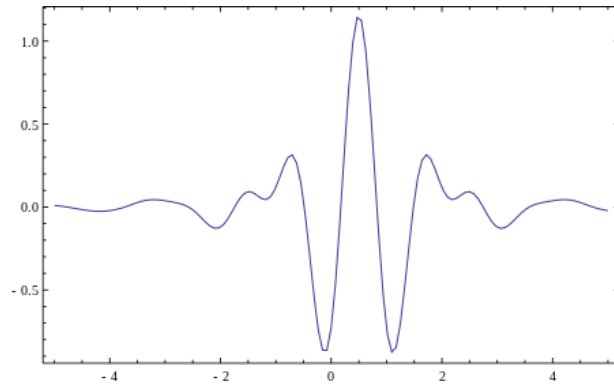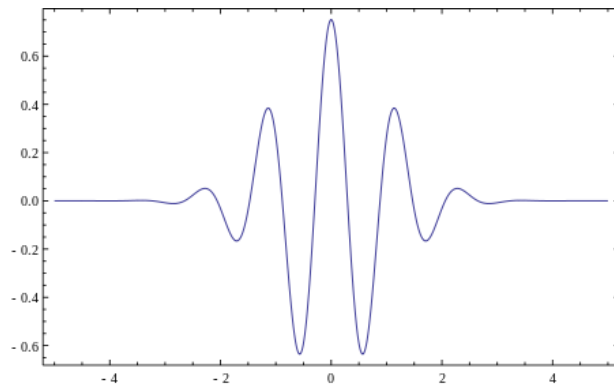
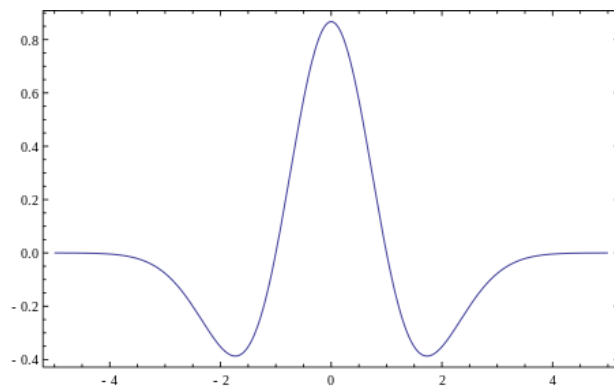Figure 2-8: Meyer wavelet

Figure 2-9: Morlet wavelet

Figure 2-10: Mexican hat wavelet

Mathematically, the complex Morlet wavelet may be described as (Chen & Chu, 2017):

$$\psi(t) = e^{i\omega_0 t}\, e^{-\frac{t^2}{2}} \qquad\qquad Eq.\ 2\text{-}19$$

Where ω_0 is the *central frequency*. To perform the wavelet transform, the mother wavelets must fulfill the admissibility condition. First, one computes the Fourier transform of the mother wavelet as:

$$\hat{\psi}(\omega) = \int_{-\infty}^{\infty} \psi(t) e^{i\omega t} \, dt$$

Eq. 2-20

From Eq. 2-20, the admissible constant, C_ψ, is defined as:

$$C_\psi = \int_0^{\infty} \frac{\left|\hat{\psi}(\omega)\right|^2}{\omega} d\omega$$

Eq. 2-21

The admissibility condition demands that $C_\psi < \infty$ (Farge, 1992), meaning that the integral of Eq. 2-21 must converge to a constant. In practice, this requires that $\omega_0 \geq 5$ (Liu P. C., 1994). If the admissibility condition is satisfied, one can compute the wavelet transform as per Eq. 2-18.

2.6   Wavelet Analysis: The dynamic criterion

To detect wave breaking, the wavelet transform has been applied in conjunction with the conventional dynamic criterion (Elsayed, 2008; Elsayed, 2011; Jinshan, Jiwei, & Enbo, 1998; Liu P. , 1993; Liu P. C., 1994; Liu & Babanin, 2004). The criterion states that the waves brakes when the downward acceleration of the fluid at the crest exceeds a ratio of the acceleration of gravity (Eq. 2-21). When applying the wavelet approach, the fluid crest acceleration is expressed as the product of the wave amplitude and the angular frequency of the fluid particle:

$$a\omega^2 = \gamma g$$

Eq. 2-22

Where a is the wave amplitude and ω is the angular frequency. Having a time-frequency wavelet energy spectrum (Jinshan, Jiwei, & Enbo, 1998):

$$E(\omega, t) = |W(\omega, t)|^2$$

Eq. 2-23

The temporally localized frequency spectrum at t_i is expressed by:

$$\Phi_i(\omega) = [E(\omega, t)]_{t=t_i} \qquad\qquad \textit{Eq. 2-24}$$

The local characteristic frequency is computed by (Rice, 1954):

$$\omega_i = \sqrt{\frac{\int_{\lambda\omega_p}^{\omega_n} \omega^2 \Phi_i(\omega) d\omega}{\int_{\lambda\omega_p}^{\omega_n} \Phi_i(\omega) d\omega}} \qquad\qquad \textit{Eq. 2-25}$$

The integral boundaries ω_p and ω_n represent respectively the peak and cut-off frequencies of the instantaneous frequency spectra. The cut-off frequency is generally set as up to 2.5 times the peak frequency (Liu & Babanin, 2004). The factor λ, introduced by Liu (1993), denotes the start of the frequency range covering the wave breaking process. Its value is not clearly defined and it has been 1.5 and 1.35 (Liu P. , 1993), solely 1.35 (Elsayed, 2008; Jinshan, Jiwei, & Enbo, 1998; Liu P. C., 1994) and 1.0 (Liu & Babanin, 2004).

Different approaches have been made to calculate the wave amplitude. Liu (1993, 1994) and Elsayed (2008) use the local wave amplitude measured directly from the time series data, *X(t)*. Jinshan (1998) computes the following characteristic amplitude:

$$a_i = \sqrt{\int_{\lambda\omega_p}^{\omega_n} \Phi_i(\omega) d\omega} \qquad\qquad \textit{Eq. 2-26}$$

Liu and Babanin (2004) theorize that an appropriate characteristic amplitude is one the form:

$$a_i = A_i \cos p_i \qquad\qquad \textit{Eq. 2-27}$$

Where:

$$A_i = |Hilbert[X(t_i)]| \qquad\qquad \text{Eq. 2-28}$$

$$p(\omega, t) = tan^{-1}\left\{\frac{Im[W(\omega, t)]}{Re[W(\omega, t)]}\right\} \qquad\qquad \text{Eq. 2-29}$$

$$p_i = [\bar{p}(\omega, t)]_{t=t_i}, \qquad \lambda\omega_p < \omega < \omega_n \qquad\qquad \text{Eq. 2-30}$$

23

The amplitude component of the characteristic amplitude, A_i, is taken as the absolute value of the Hilbert-transformed surface elevation data. The wavelet phase spectrum, $p\ (\omega,\ t)$, is calculated as the angle between the complex and real components of the time-frequency wavelet spectrum $W\ (\omega,\ t)$, whence the local characteristic phase, p_i, is obtained from averaging the local phase spectrum with the same range as with the characteristic frequency (Babanin A. V., 2011). This approach requires the mother wavelet to be complex to obtain the temporally localized phase spectra.

2.7   Wavelet Transform: Local Energy Density

If $\psi(t)$ is real and admissible, the original signal can be restored by the inverse wavelet transform (Chen & Chu, 2017):

$$X(t) = \frac{1}{C_\psi} \int_0^\infty \int_{-\infty}^\infty W_{X\psi}(s,t') \frac{1}{\sqrt{s}} \psi\left(\frac{t-t'}{s}\right) dt' \frac{ds}{s^2} \qquad Eq.\ 2\text{-}31$$

Parseval's theorem states that the integral of a function's square modulus is equal to the integral of the square modulus of the same function in frequency domain. As with conventional Fourier transform, the total energy of the signal is conserved when wavelet-transformed. Parseval's theorem can therefore be rewritten as (Chen & Chu, 2017):

$$\int_{-\infty}^\infty |X(t)|^2 dt = \frac{1}{C_\psi} \int_0^\infty \int_{-\infty}^\infty |W_{X\psi}(s,t')|^2 dt \frac{ds}{s^2} \qquad Eq.\ 2\text{-}32$$

Integrating the wavelet spectrum with respect to frequency provides temporal information on the variation of the localized total energy (Liu P. , 1993). Liu observes that the peaks of the local energy density spectrum correlate with breaking events. Figure 2-11 compares the occurrence of breaking events with the temporally localized energy density. The upper graph depicts an excerpt of the wave record. The circles mark the occurrence of breaking events after the dynamic criterion with two different values for λ (Eq. 2-26). The lower graph depicts the integrated wavelet spectrum over frequency. From the results of Liu, one observes that the energy density peaks point to certain circles marking the breaking events. The local energy density spectrum seems to identify and distinguish the groupings of the wave data. Elsayed (2008, 2011) came to the same conclusions in his papers.
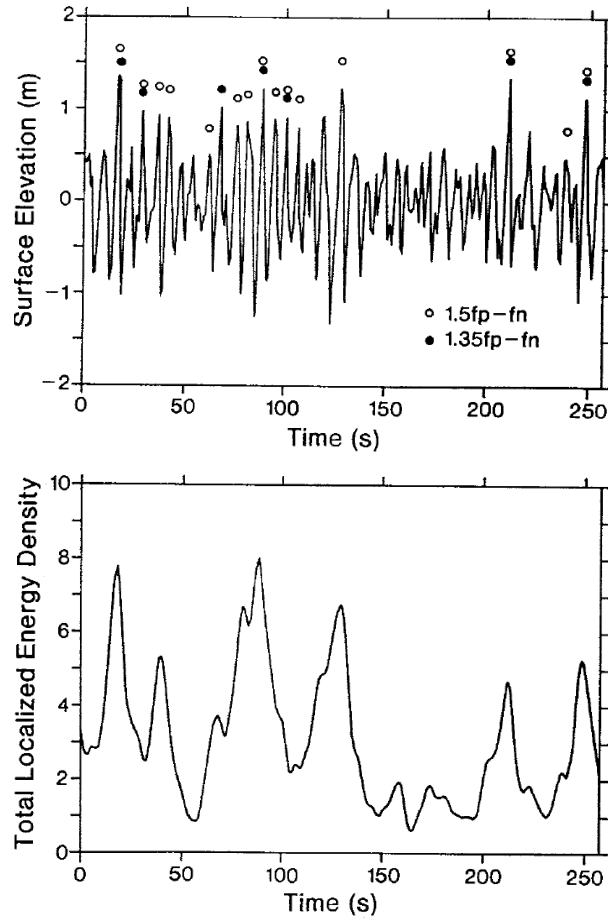
Figure 2-11: Local energy density peaks and breaking events (Liu P. , 1993).

Other than "integration of the wavelet transform over frequency" (Elsayed, 2008, p. 276; Liu, 1993, p. 971) the articles do not specify the applied mathematical formulation. Massel (2001) elaborates on the expressions for the different wavelet energy spectra. Firstly, the time-scale energy density is expressed as the following:

$$E_1(\tau, b) = \frac{|WT(\tau, b)|^2}{b} \qquad \text{Eq. 2-33}$$

Where τ is the time shift and b is the scale factor (equivalent to frequency). It is worth to mention that this expression of energy is normalized by the scale factor, as opposed to Eq. 2-23. From Eq. 2-33, the *local energy density* is found by integrating over the scale:

$$E_2(\tau) = \frac{1}{C} \int_0^\infty E_1(\tau, b) \frac{db}{b} \qquad \text{Eq. 2-34}$$

25

Where C is the admissibility constant and E_2 correspond to the total localized energy density spectrum (Figure 2-11) of which its peaks may indicate the temporal location of wave breaking. Eq. 2-33 may also yield the *global wavelet energy spectrum* which is calculated by:

$$E_3(b) = \int_0^\infty E_1(\tau, b) \, d\tau \qquad \text{Eq. 2-35}$$

When applying the FFT on a time series, the very jagged spectrum approaches the shape of E_3 when smoothed (Torrence & Compo, 1998). Finally, the total energy is found by:

$$E_{tot} = \frac{1}{C} \int_0^\infty E_3(b) \frac{db}{b} \qquad \text{Eq. 2-36}$$

The total energy of the wavelet-transformed signal is conserved can be calculated from:

$$E_{tot} = \frac{1}{C} \int_0^\infty \int_{-\infty}^\infty E_1(\tau, b) \frac{d\tau db}{b} = \frac{1}{C} \int_0^\infty \int_{-\infty}^\infty |WT(\tau, b)|^2 \frac{dt \, ds}{s^2} \qquad \text{Eq. 2-37}$$

3   Methodology

An extensive set of data is received from a wave tank model at MARINTEK in Trondheim. The waves are modeled as long-crested deep-water waves with a Froude scale of 1:55. The experiment has been realized 20 times with each realization lasting for approximately 3 hours and 15 minutes after Froude scaling. The surface elevation is measured by 23 gauges with a distance of 15 centimeters in between them, as depicted in Figure 3-1. This chapter describes the methodology applied to calculate the different wave breaking parameters and criteria as described by the previous chapter.

Figure 3-1: Set up of wave gauges at MARINTEK wave tank

3.1   Pre-processing of Data

First, the time series data from a realization is loaded into MATLAB. This set of data contains the measurements of all 23 wave gauges, i.e. the surface elevations and the corresponding time instants. Each gauge has a sampling rate of 1 200 Hz which yields over 1.9 million data points over the run of a realization. As such extensive data set is overly detailed and computationally expensive, the sampling rate is reduced to 100 Hz. This is done by defining the array of time instants as *0:dt:t$_{fin}$* with *dt = 0.01*. The corresponding surface elevation data is reduced by interpolation using the *interp1*-function by applying the spline method.

After down sampling, the data is scaled from model scale to full scale by using the Froude scaling factor. The surface elevation data is multiplied with 55 while the corresponding time instants are multiplied with the square root of 55. As the time of the final time instant has increased by the multiple of the square root of 55, yet the number of data points remains constant, the effective sampling rate is consequently reduced to approximately 13.5 Hz. The

last manipulation of the data involves the omission of the 50 first seconds of the time series which constitute the ramp-up period of the test.

By the *zeroup_new* function, the entire time series is discretized into a series of wave events, each indexed by a number, *nw*. In addition, the function computes the wave height, wave period, amplitude of trough, amplitude of crest, and the time instant of the crest amplitude. The first realization registers 849 wave events. The *wavenumber* function assumes linear wave theory and computes the wavenumber and wavelength of a wave event given its wave period.

3.2   Geometric Criterion

The geometric criteria concern with the geometrical properties of the wave amplitude and theorizes that a wave will eventually break if the amplitude becomes too steep. The geometric criterion is chosen to be defined by the steepness factor, *ka* having that Stokes limiting criterion is suited for vertically symmetric waves. The threshold is set as *0.44* which has been found to be robust by Toffoli *et al*. (2010). Since some recognized wave events by the *zeroup_new-* function are very short and almost completely flat, an additional criterion of a wave height over 1 meter is demanded. Thus, from the geometric criteria, waves fulfilling the following conditions are searched for:

$$ka \geq 0.44 \ \cap h > 1 \, m$$

Where *k* is the wavenumber, *a* is the crest amplitude and *h* is the wave height.

3.3   Kinematic/Dynamic Criteria

The kinematic criteria hypothesize that a wave will overturn when the crest velocity exceeds the phase velocity. Similarly, an energy principle labelled under the dynamic criteria states that the energy a wave can consume from its neighboring waves has an upper limit. If this threshold is met or exceeded, the wave will break. At the free surface, this threshold manifests itself as the ratio between the crest velocity and phase speed. Eq. 2-19 is used for calculating the ratio. By applying the *hilbert*-function one gets:

$$H(t) = Hilbert[\zeta(t)] = \zeta(t) + i\xi(t)$$

Where $\zeta(t)$ is the surface elevation data. The horizontal particle velocity is computed as:

$$u(t) = \frac{d\xi(t)}{dt}$$

Where the difference is computed by the *diff*-function. The instantaneous angular frequency is calculated by using the *instfreq*-function and multiplying the resulting time series with 2π:

$$IF(t) = instfreq(\zeta(t), SF, 'Method', 'hilbert')$$
$$\omega(t) = 2\pi * IF(t)$$

Where SF is the sampling frequency. Thus, the kinematic criterion as defined by the instantaneous wave properties, are calculated by

$$\frac{u(t)\,\omega(t)}{g} > 0.8$$

3.4 Dynamic Criterion, Euler acceleration

Based on the idea of Longuet-Higgins and Smith, and by recommendation from Tęgowski, the double time derivative of the surface elevation with respect to time is calculated. According to Tęgowski, the double derivate is "very sensitive to the rate of surface local slope variation". Hence, this dimension may be a good indicator for wave breaking. The first time derivative is calculated by:

$$v = \frac{d\eta}{dt} = \frac{(\eta_n - \eta_{n-1})}{(t_n - t_{n-1})}$$

Where v is the temporal rate of variation which expresses the slope at the evaluated points, η_n is the n-th data point of the surface elevation and t_n is the corresponding time instant. The second time derivative is calculated by

$$a_E = \frac{d^2\eta}{dt^2} = \frac{(v_n - v_{n-1})}{(t_n - t_{n-1})}$$

Where a_E is the Euler acceleration at the free surface and expresses the rate of variation of the slope v. The differentiation of the array elements is calculated by applying the *diff* function.

3.5 Wavelet Transform: The Dynamic Criterion

This approach is following the method of Liu and Babanin (2004) as described in section 2.6. Firstly, the time series is converted into the data type *double*. This is because the *cwt-*function that performs the wavelet transform does not admit data of type *single*. The wavelet coefficients *CWT* and at the belonging frequencies *F* is then calculated by:

$$[CWT(f,t),F] = cwt(\eta(t), SF,'amor','NumOctaves', No,'VoicesPerOctave', Nvpo)$$

Where $\eta(t)$ is the surface elevation time series, *SF* is the sampling frequency and *amor* specifies using the analytic Morlet wavelet. The number of octaves specifies for which range of frequencies the transform is computed by and the voices per octave can be thought as the resolution of the transform. It is found that for this data that 8 octaves gives the relevant frequency limits and the number of voices per octave is set to be 48 which is the highest permissible resolution. The energy density spectrum is defined as the magnitude squared of the wavelet coefficients:

$$E_{CWT}(f,t) = |CWT(f,t)|^2$$

Then three limiting criteria are set as:

$$\gamma = 0.5, \qquad \lambda = 1, \qquad \frac{f_{cut}}{f_{peak}} = 1.5$$

Where their significance and justification are elaborated in section 4.4. The peak and cut-off frequencies are then found for all time instant to find their average frequency. The spectral moments limited by the peak and cut-off frequencies are calculated as a Riemann sum for every time instant t_i:

$$m_0(t_i) = \sum_{f=f_{peak}}^{f_{cut}} E_{CWT}(f, t_i) \Delta f$$

$$m_2(t_i) = \sum_{f=f_{peak}}^{f_{cut}} E_{CWT}(f, t_i) \Delta f \cdot f^2$$

The average angular frequency is calculated by:

$$\omega_{avg}(t) = 2\pi f_{avg}(t) = \sqrt{\frac{m_2(t)}{m_0(t)}}$$

Then it remains to determine the characteristic amplitude. The analytical envelope of the surface elevation A is found by:

$$A(t) = |Hilbert[\eta(t)]|$$

The corresponding phase spectrum to the energy spectrum is defined by the angle between the complex and real components of the wavelet coefficients.

$$p(f, t) = atan\left\{\frac{I[CWT(f, t)]}{R[CWT(f, t)]}\right\}$$

The angles are calculated by using the function *atan* as it always outputs an angle between $[-\pi/2, \pi/2]$ contrary to *angle* and *atan2*. The instantaneous angle at time t_i as a mean within the same range for the average frequency such that:

$$p(t_i) = \frac{1}{f_{cut} - f_{peak}} \sum_{f=f_{peak}}^{f_{cut}} p(f, t_i)$$

The local characteristic amplitude is calculated by:

$$a(t) = A(t) \cos[p(t)]$$

Breaking events are then found for:

$$a(t)\, \omega(t)^2 \geq \gamma g$$

Where γ is the limiting factor and g is the acceleration of gravity.

3.6   Wavelet Transform: Local Energy Density

The wavelet coefficients are calculated in the same manner as in the previous section. The total localized energy density is found by summing all spectral densities over the entire frequency spectra. For a given time instant, the local energy density is found as:

$$E_{local}(t_i) = \sum_{n=1}^{385} E_{CWT}(f_n, t_i)$$

As *cwt* yields 385 data points for each frequency spectrum. The limiting criterion to find breaking event is formulated as the following:

$$E_{local}(t) \geq \gamma E_{local}^{max}(t)$$

Where the limiting threshold γ is determined in section 4.5.

3.7   Detection of Wave Breaking

When waves fulfill one (or more) of the abovementioned criteria, these waves are further inspected for breaking. The surface elevation fulfilling a criterion is plotted with its recordings by the neighboring wave staffs. An example of an identified breaking wave by this method is

graphed in *Figure* 3-2. The evident collapse of the wave crest is a clear indication of a breaking wave event. Xu *et al.* (1998) mention that when waves break, water particles at the surface jump into air, thus giving the wave surface singular points. They also convey that singularities occur when the surface elevation forms very nonlinear sharp peaks. However, visual inspection by video capture remains the only definite way of ensuring that wave breaking occurs.
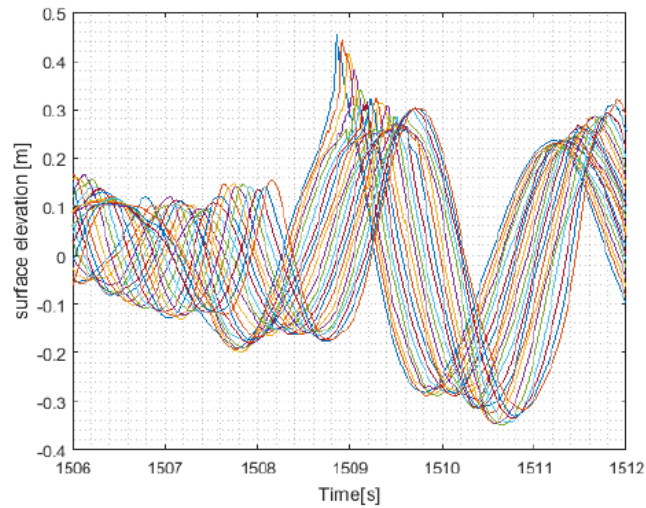

Figure 3-2: Occurrence of wave breaking

The robustness of the criteria will be measured by the following metrics:

$$Detection\ Rate\ (DR) = \frac{Detected\ wave\ events\ identified\ as\ breaking}{Detected\ wave\ events} \cdot 100\ \%$$

$$Rate\ of\ False\ Positives\ (RFP) = \frac{Detected\ wave\ events\ identified\ as\ non\ breaking}{Detected\ wave\ events} \cdot 100\ \%$$

$$Probaility\ (P) = \frac{Detected\ wave\ events\ identified\ as\ breaking}{All\ wave\ events} \cdot 100\ \%$$

Where "detected wave events" signifies waves exceeding the different threshold values.

4 Results and Discussion

4.1 Geometric Criterion

From the methodology described in section 3.2, the script recognizes 19 breaking events. Upon visual inspection, only 7 of them considered to be actual breaking events. Figure 4-1 depicts four wave events measured by all 23 wave gauges. The title of the figure gives the calculated steepness factor and the number of wave. The wave events beneath the red circle are the wave events in question.
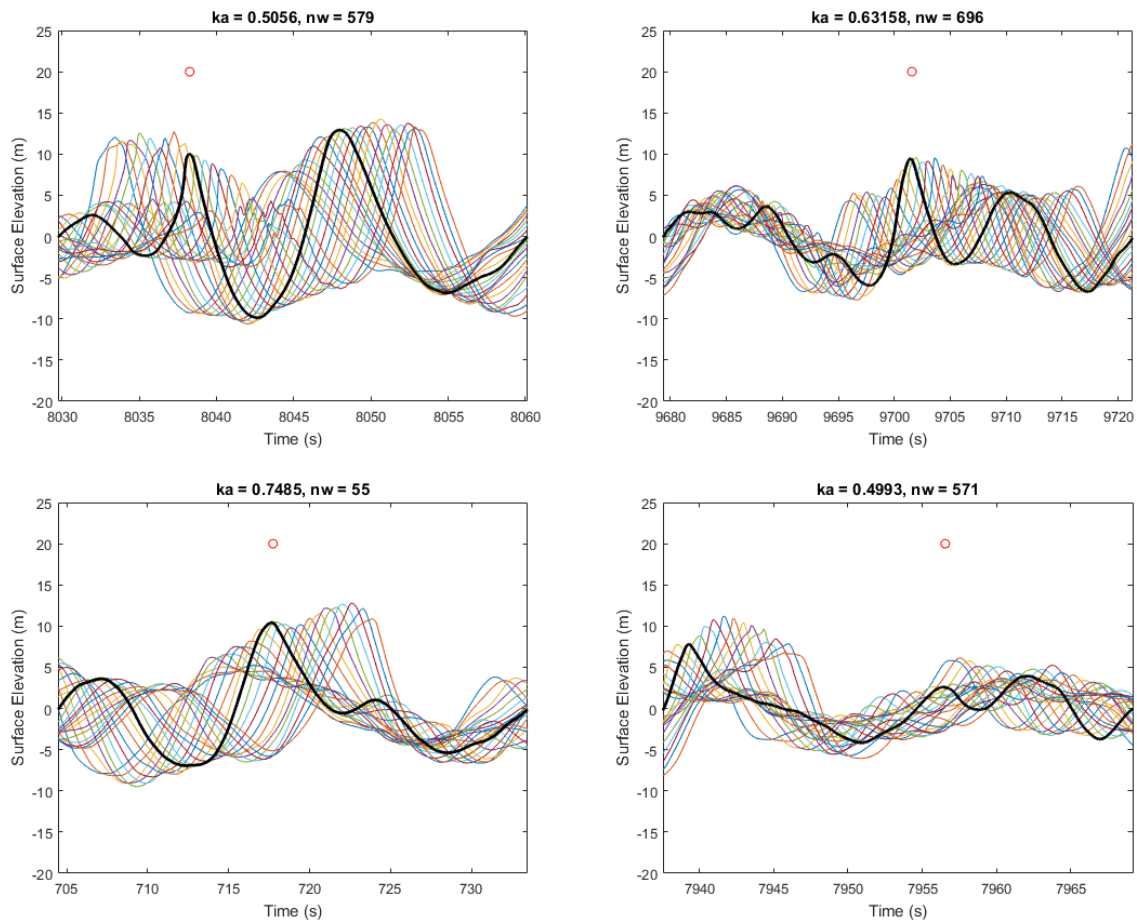

Figure 4-1: Breaking and non-breaking events by the geometric criterion

The first row corresponds to wave events considered to be breaking, and it is determined by looking at the descent and disintegration of the wave crest. The second row depicts waves that are not considered to be breaking events, at least not when passing the gauges. Looking at their *ka*-value, they both shall break according to the literature, and they can be in early phase of breaking, especially *nw = 55*. However, incipient breaking events are hard to evaluate by this method and the formation and development of the surface elevation given at the figures indicate

that neither white capping, spilling nor plunging are occurring. The incidence of all suspected breaking events is marked by a red circle in Figure 4-2. "Confirmed" breaking events, are marked by a black cross under certain red circles.
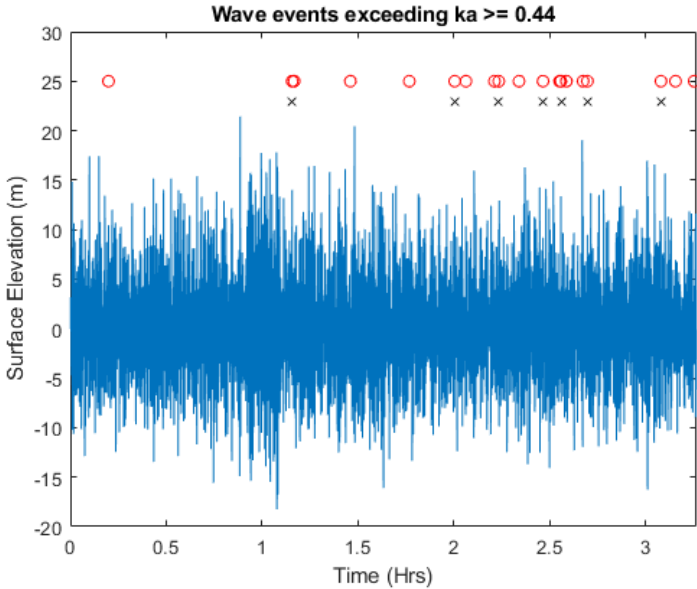

Figure 4-2: Surface elevation with marked breaking events after geometric criterion

From section 3.7, the detection rate and rate of false positive are found to be respectively:

$$DR = 36.8\,\%$$
$$ROFP = 63.2\,\%$$
$$P = 0.82\,\%$$

The great advantage of this method is that it is relatively easy to implement, but the positive qualities of this method stops at this. With a detection rate of only 36.8 %, i.e. the percentage of actual breaking waves over the number of waves fulfilling the geometric criterion, this method is deemed highly inaccurate. Subsequently, the rate of false positives, i.e. non-breaking waves fulfilling the geometric criterion, is at 63.2 %. Many of the detected waves have also a high steepness number, without to seem to break given their graphical representations in the plots. This might be due to the criterion, at least in this analysis, uses the linear relationship between the wavelength and wavenumber which does not reflect the true properties of these often highly irregular wave trains.

35

This method performs very poorly as it finds only 7 breaking events out of 849 total wave events, which estimates that breaking waves has a frequency of 0.82 % for this realization. The objective of this thesis is to find a fast, reliable, and accurate method to detect breaking events, and the steepness factor fails to do this. It is recommended that this method is not applied for analyzing time series of surface elevation as the results yield poor detection and accuracy. A suggestion is that this method may be applied for data when the surface elevations are given in space domain, which may be facilitated by numeric simulations.

4.2   Kinematic Criterion

An attempt to inspect for breaking waves after the kinematic criterion where the velocities are defined by the phase-time method is unsuccessful. The resulting plot represents the kinematic criterion as per Eq. 2-14:
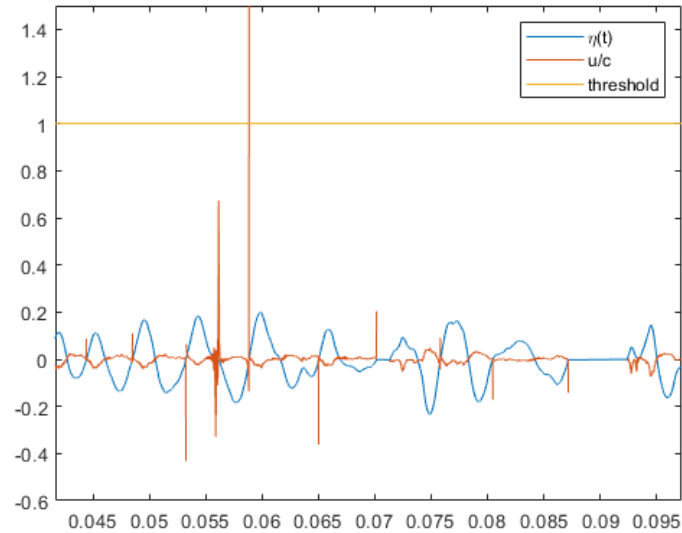

Figure 4-3: Kinematic criterion by phase-time method

The segmentation of the time series is due a discrimination of all wave events with wave crests near the mean water line as recommended by Zimmerman and Seymour (2002). When computing the instantaneous frequency by applying the Hilbert-transform, they demonstrate mathematically that the instantaneous frequency becomes very large when the original signal is near zero. In essence, the instantaneous frequency is inversely proportional to the original signal squared, which is the surface elevation in this case. The entire surface elevation is therefore segmented into their wave events. As recommended by Zimmerman and Seymour, wave events with a wave height lower than *0.38H_s* are omitted. As the *hilbert*-function only admits continuous signals, the surface elevation is transformed one wave event at the time and the instantaneous frequencies are stitched back together at last.

From Figure 4-3: Kinematic criterion by phase-time method, it is observed that singularities that satisfies the kinematic criterion occurs only at the up-crossing and down-crossing of the surface elevation. This might be due to ill-conditioning of the signal and that the denominator somewhere in the scripts takes a value close to zero. In this work, the kinematic criterion is not further explored.

4.3   Dynamic Criterion

From the method described in the methodology, the velocities and accelerations at the free surface (Euler acceleration) are found to be as in Figure 4-4. It seems that certain accelerations are exceeding 200 m/s^2 which is deemed illogical. Transients at the surface elevation data result in very high second derivatives.
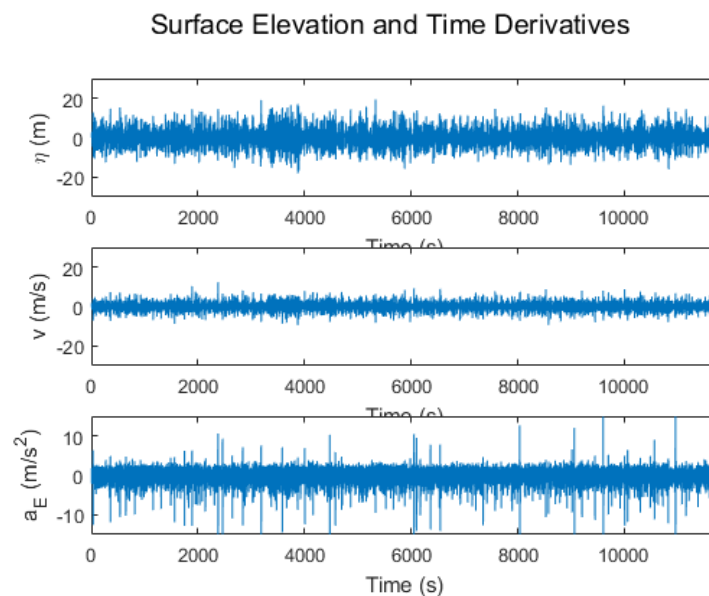

Figure 4-4: Surface elevation with first and second time derivatives

To counter this, the surface elevation is filtered by a moving average filter by using *filter* and 20 as the window size. The smoothed surface and its corresponding second derivative are shown in Figure 4-5. The acceleration is graphed in orange and is normalized by the acceleration of gravity. The smoothed surface elevation is blue and is reduced by a factor of 10. As expected from linear wave theory, the highest downward accelerations occur at the wave crests and the troughs exhibit upward accelerations as in Figure 2-4. However, the acceleration shown in this plot is noisy and the large acceleration at *2380 s* is transient.
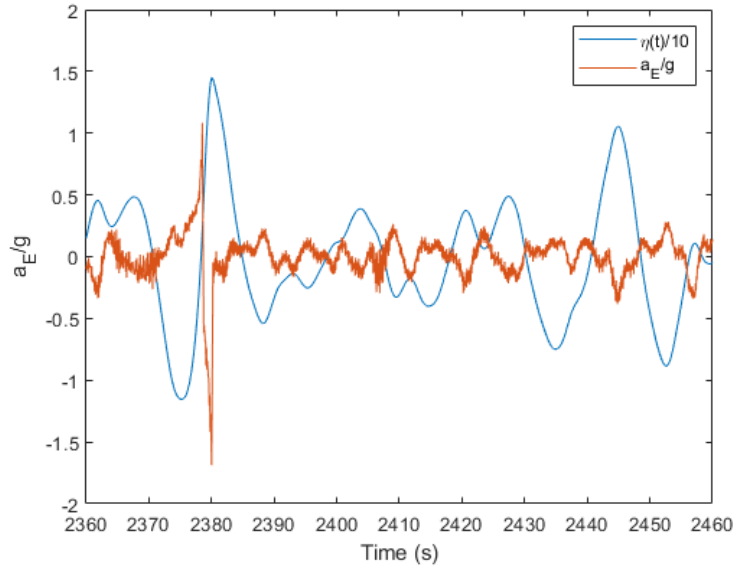
Figure 4-5: Smoothed surface elevation and Euler acceleration

Therefore, another smoothing is made. The acceleration seen in Figure 4-5 is smoothed by the same window as for the surface elevation, and the resulting acceleration graphed in Figure 4-7:
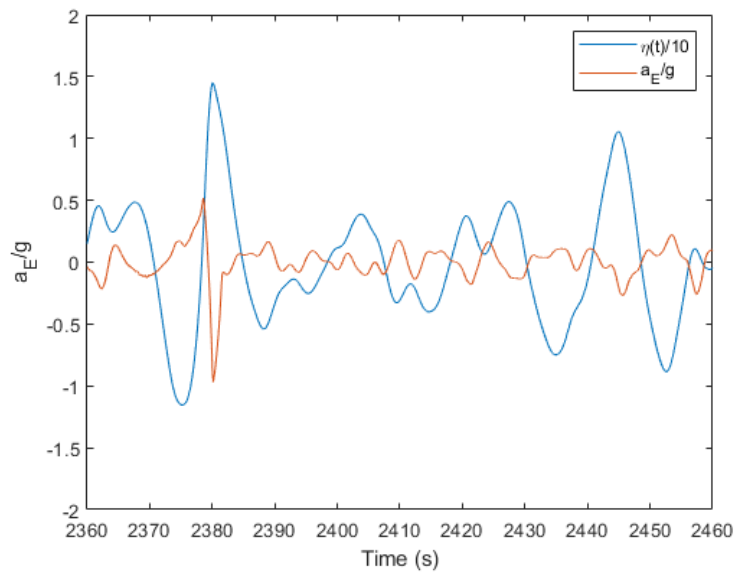

Figure 4-6: Smoothed surface elevation with smoothed acceleration

The figure shows that the normalized acceleration finally has a smooth oscillation. This acceleration is considered more realistic and closer to the real acceleration than the acceleration from the non-filtered data. The dynamic criterion is calculated as:

$$\frac{a_E}{g} = \gamma$$

Where γ is the limiting criterion, typically established empirically in experiments and simulations. The onset of breaking has classically been determined when γ is between *- 0.3* and *- 0.4*. In the MATLAB script, setting γ to be *-0.4* gives 148 wave events suspected to break. It is therefore decreased to *-0.7* which yields 31 events (in the first realization). The dynamic criterion can be visualized as in Figure 4-7:
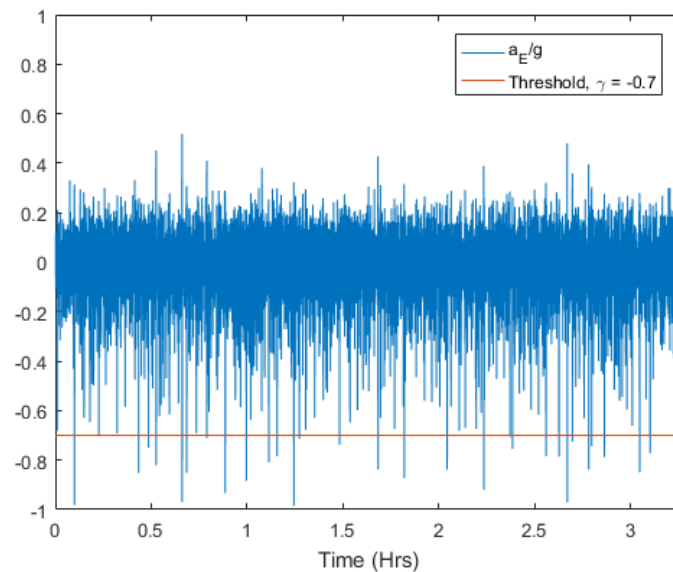

Figure 4-7: Dynamic criterion

In Figure 4-8 on the following page, two of the 31 wave events that are considered to break are represented in the first row. Two wave events considered non-breaking are represented in the second row. The top row clearly shows wave events in the process of breaking. One can tell by the steep wave crests, their rapid descent over time, and the disintegration of the water surface. The bottom row demonstrates only tall waves, but none of the other properties. These waves may be in an early process of breaking, but a clear tendency of actual breaking is not recorded by the gauges and they are therefore not considered as breaking waves.
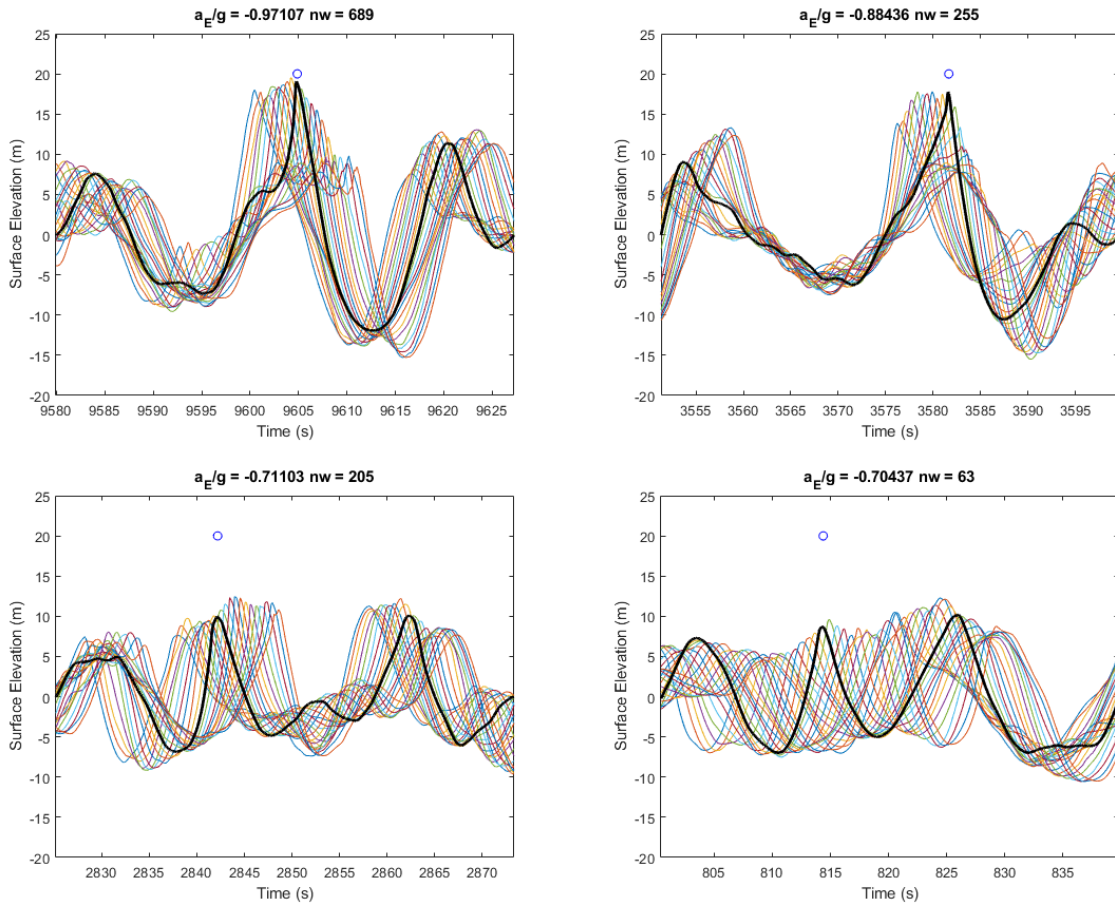
Figure 4-8: Breaking and non-breaking events by the dynamic criterion

The occurrence of all wave events detected by the dynamic criterion are displayed in Figure 4-9. All detected waves by this criterion are marked by blue circles and the confirmed breaking events upon visual inspection are marked by black crosses.
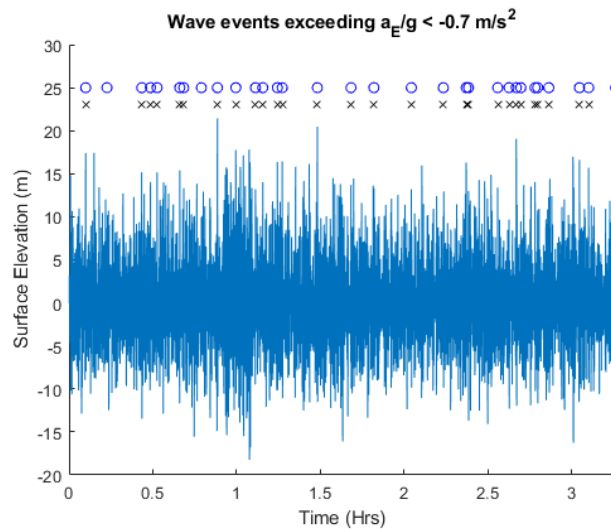

Figure 4-9: Surface elevation with marked breaking events after dynamic criterion

Figure 4-9 shows that the waves detected by this criterion and actual breaking waves are highly coinciding. The resulting performance parameters are calculated to be:

$$DR = 90.3\,\%$$
$$ROFP = 9.7\%$$
$$P = 3.3\%$$

This method is regarded to be very accurate as 90.3 % of all detected waves is considered to be actual breaking. Consequently, this method yields a low rate of false positives where even certain false positives can be argued to be considered as breaking waves. This method captures a high number of breaking events relative to the total number of wave events, namely 3.3 %.

Clearly, the dynamic criterion by this method has many positive attributes. Besides having a great performance, it is easy to implement and identify wave events with clear breaking characteristics. However, this method may describe the geometry and the rate of change of the surface of wave events, rather than the actual acceleration of the water particles at the free surface. Furthermore, the window size of the filtration scheme of the data is somewhat arbitrary and a more critical approach to treat the data may result in a better performance of this method. Also, it can be interesting to observe how the performance of this method varies when the threshold value is set higher and lower.

4.4 Wavelet Analysis: Dynamic Criterion

Three parameters have been varied to study which combination yields a sensible number of suspected breaking waves, i.e. waves satisfying the dynamic criterion by the mathematical formulation. These parameters are γ, λ and the considered frequency range of the integral. These factors are related by:

$$a\omega_{avg}^2 \geq \gamma g, \qquad \omega_{avg} = 2\pi f_{avg}^2, \qquad f_{avg} = \frac{\sqrt{\int_{\lambda f_p}^{f_{cut}} f^2 E_{CWT}(f) df}}{\sqrt{\int_{\lambda f_p}^{f_{cut}} E_{CWT}(f) df}}$$

Where E_{CWT} (f) is the local frequency spectrum at given time instant obtained by continuous wavelet transform. The parameters are varied for λ = {1, 1.35, 1.5}, γ = {0.3, 0.4 0.5}, and f_{cut}/f_{peak} = {1.5, 2.0, 2.5}. In Table 4 where $\lambda = f_{cut}/f_{peak}$ = 1.5, the average frequency f_{avg} does not compute. Otherwise, it is observed that the number suspected wave breaking events increases when the frequency range increases and when the onset of the range is increases. The number is decreasing for increasing threshold value γ.
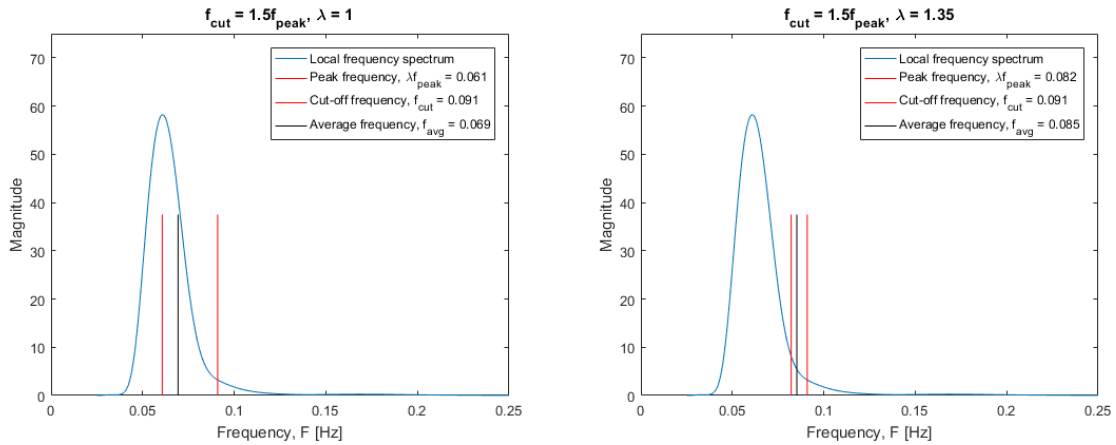

Figure 4-10: Range of frequencies, f_{cut} = 1.5 f_{peak}

Table 4: No. of suspected breaking waves, $f_{cut} = 1.5 f_{peak}$ with varying λ and γ

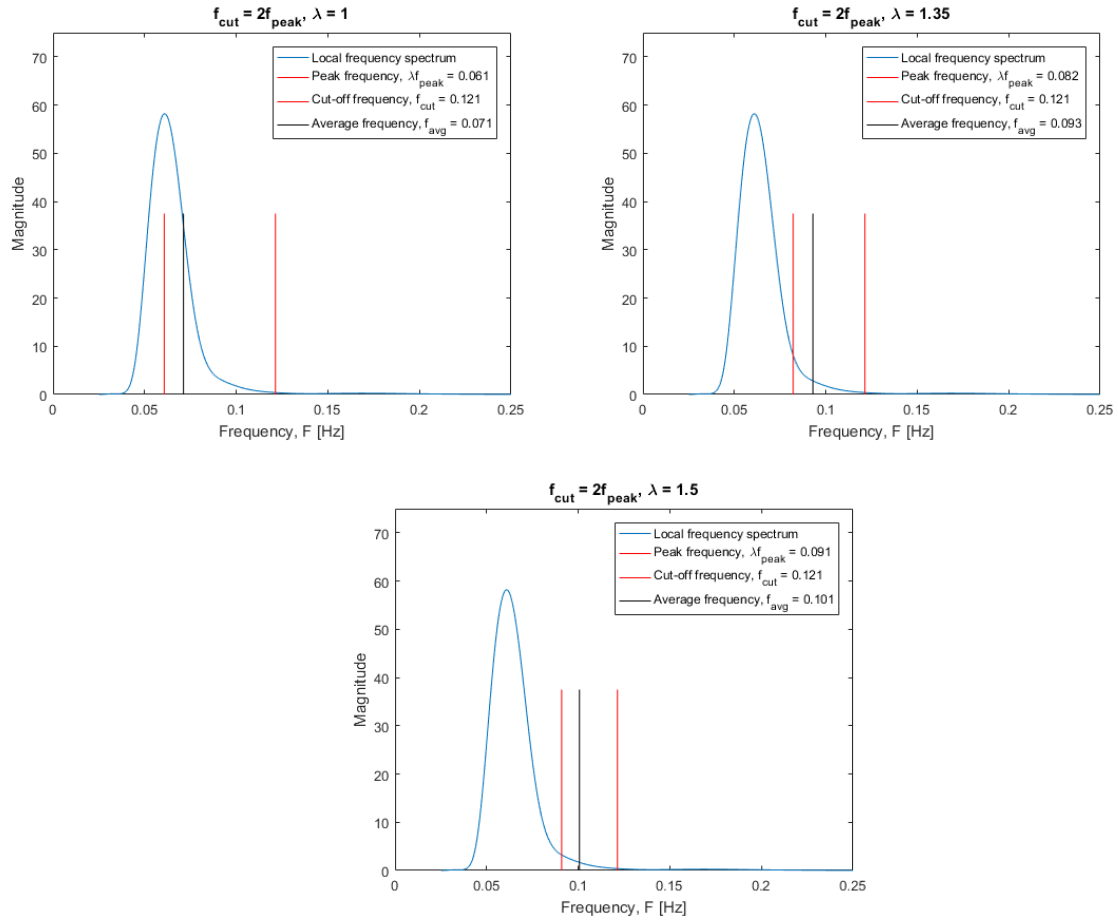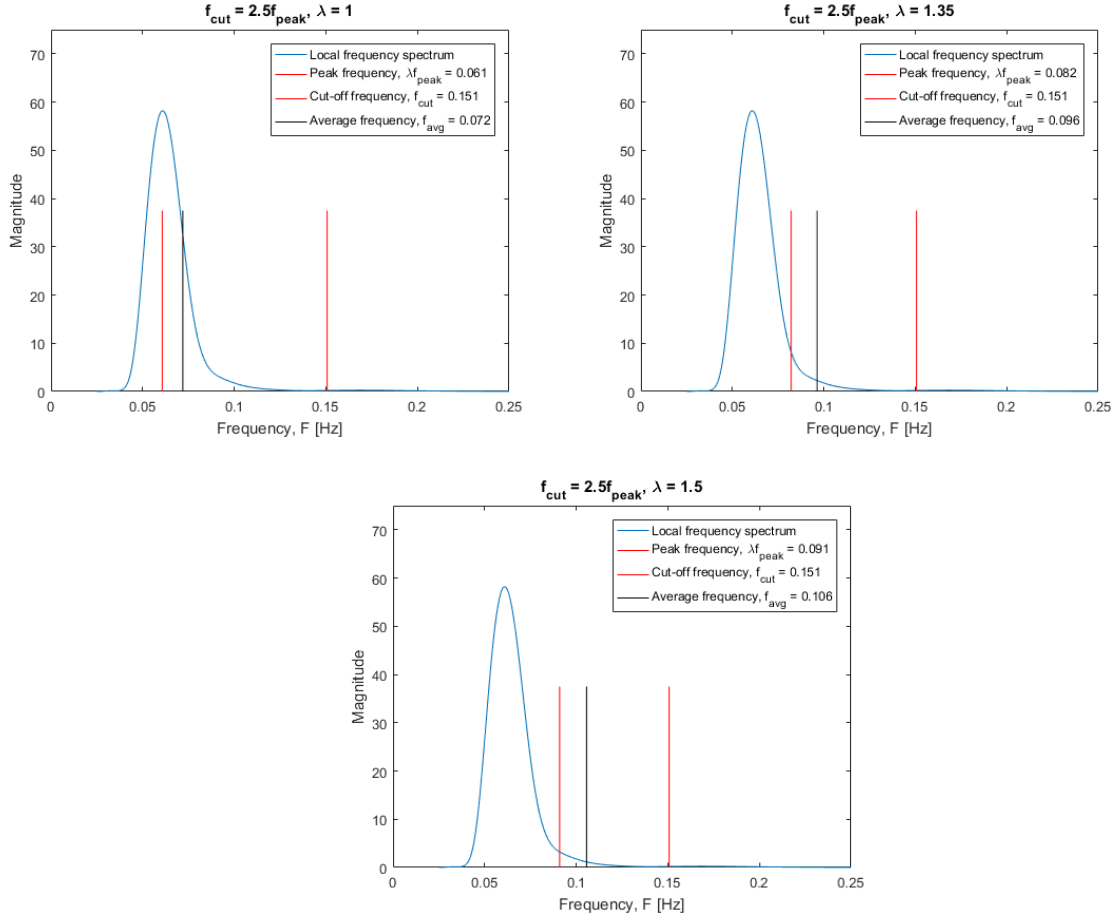|	γ		
λ	0.3	0.4	0.5
1	70	19	4
1.35	167	83	36
1.5	-	-	-

Figure 4-11: Range of frequencies, $f_{cut} = 2 f_{peak}$

Table 5: No. of suspected breaking waves, $f_{cut} = 2f_{peak}$ with varying λ and γ

	γ		
λ	0.3	0.4	0.5
1	112	39	9
1.35	351	169	89
1.5	409	250	137

44

$f_{cut} = 2.5f_{peak}$, $\lambda = 1$

Magnitude

- Local frequency spectrum
- Peak frequency, $\lambda f_{peak} = 0.061$
- Cut-off frequency, $f_{cut} = 0.151$
- Average frequency, $f_{avg} = 0.072$

Frequency, F [Hz]

$f_{cut} = 2.5f_{peak}$, $\lambda = 1.35$

Magnitude

- Local frequency spectrum
- Peak frequency, $\lambda f_{peak} = 0.082$
- Cut-off frequency, $f_{cut} = 0.151$
- Average frequency, $f_{avg} = 0.096$

Frequency, F [Hz]

$f_{cut} = 2.5f_{peak}$, $\lambda = 1.5$

Magnitude

- Local frequency spectrum
- Peak frequency, $\lambda f_{peak} = 0.091$
- Cut-off frequency, $f_{cut} = 0.151$
- Average frequency, $f_{avg} = 0.106$

Frequency, F [Hz]

Figure 4-12: Range of frequencies, $f_{cut} = 2.5\, f_{peak}$

Table 6: No. of suspected breaking waves, $f_{cut} = 2.5f_{peak}$ with varying λ and γ

	γ		
λ	0.3	0.4	0.5
1	157	55	16
1.35	459	270	141
1.5	525	353	221

Figure 4-10, Figure 4-11 and Figure 4-12 visualize how the average frequency increases when increasing γ and λ, ultimately yielding a higher detection rate. The red bars marks where the frequency range begins and ends, i.e. the limits of integration, and the black bar correspond to the resulting average frequency. For a given f_{cut}/f_{peak}-ratio, the cut-off frequency (rightmost bar) is fixed relative to the peak of the frequency spectrum and does not shift when λ increases. The average frequency is greatly affected when moving the onset of the frequency range closer to the cut-off frequency, as can be seen in all three figures. The frequency is typically increasing

from approximately $f \approx 0.071\ Hz$ to $f \approx 0.0103\ Hz$. Fixing λ and broadening the range have a smaller impact on the average frequency, however there is still a consistent and increasing trend, as can be seen in Table 7:

Table 7: Resulting average frequency from varying frequency range and λ

f_{cut}/f_{peak}	λ		
	1.0	1.35	1.5
1.5	0.069	0.85	-
2.0	0.071	0.093	0.101
2.5	0.072	0.096	0.106

From the figures, it is observable that the contribution of the high-frequency range is small having that this particular frequency spectrum has a steep decline after its peak frequency. All 158 345 local frequency spectra calculated by the *cwt*-function do not exhibit this shape. For instance, spectra having a more trapezoidal shape will have a great contribution from the high-frequency range and consequently contribute to detect a high number of breaking waves.

In "Using wavelet spectrum analysis to resolve breaking events in the wind wave time series" (Liu & Babanin, 2004), the selected combination of the three parameters are: $\lambda = 1$, $\gamma = 0.3$, and $f_{cut}/f_{peak} = 2.5$. From Table 6, this reads 157 detected wave breaking events in this analysis. As $\gamma = 0.3$ gives a high number of breaking events for all frequency ranges, this study will further explore breaking events when $\gamma = 0.4$. The frequency range and λ is set as $f_{cut}/f_{peak} = 2$ and $\lambda = 1$ as in the article.

When using the *cwt*-function on the time series data with specified sampling rate, mother wavelet, number of octaves and voices per octaves, the graphs in Figure 4-13 are obtained. The magnitude scalogram shows the time-frequency domain of the local phase spectra. The global wavelet spectrum is calculated per Eq. 2-33 and Eq. 2-34 and is normalized by the number of data points. This measure finds the most typical frequency of which the surface elevations consists. The experimental realization generated waves with $t_p = 2.75\ s$. After inversion and Froude-scaling the corresponding peak frequency becomes $f_p = 0.0490\ Hz$. The peak frequency of the global wavelet spectrum is $f_p^{wavelet} = 0.0503\ Hz$, which is considered a small deviation. The transform is therefore considered to be performed correctly.
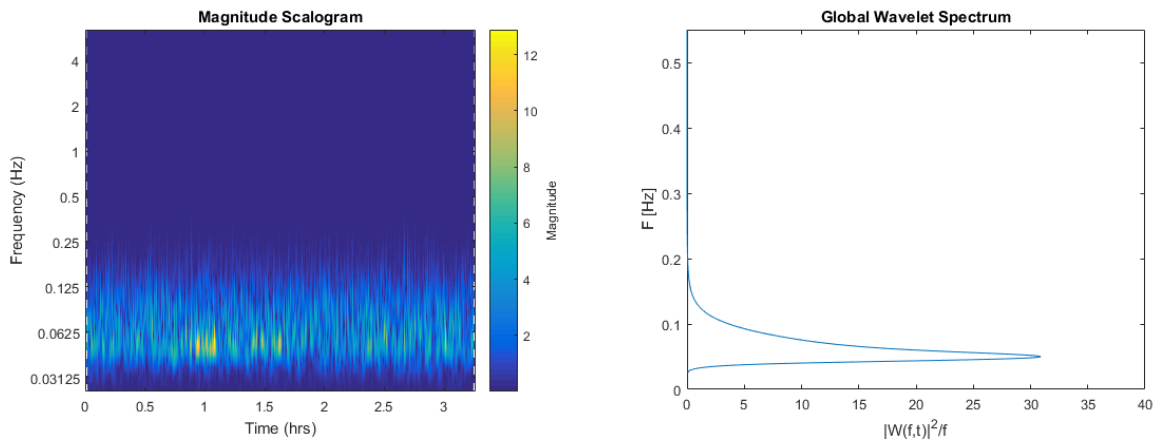
Figure 4-13: Wavelet transform: Magnitude scalogram and global wavelet spectrum

Figure 4-14 compares the magnitude scalogram to the surface elevation. From the figure it is read that the highest magnitudes occur where the surface elevation is at its highest and be is a part of a wave group.
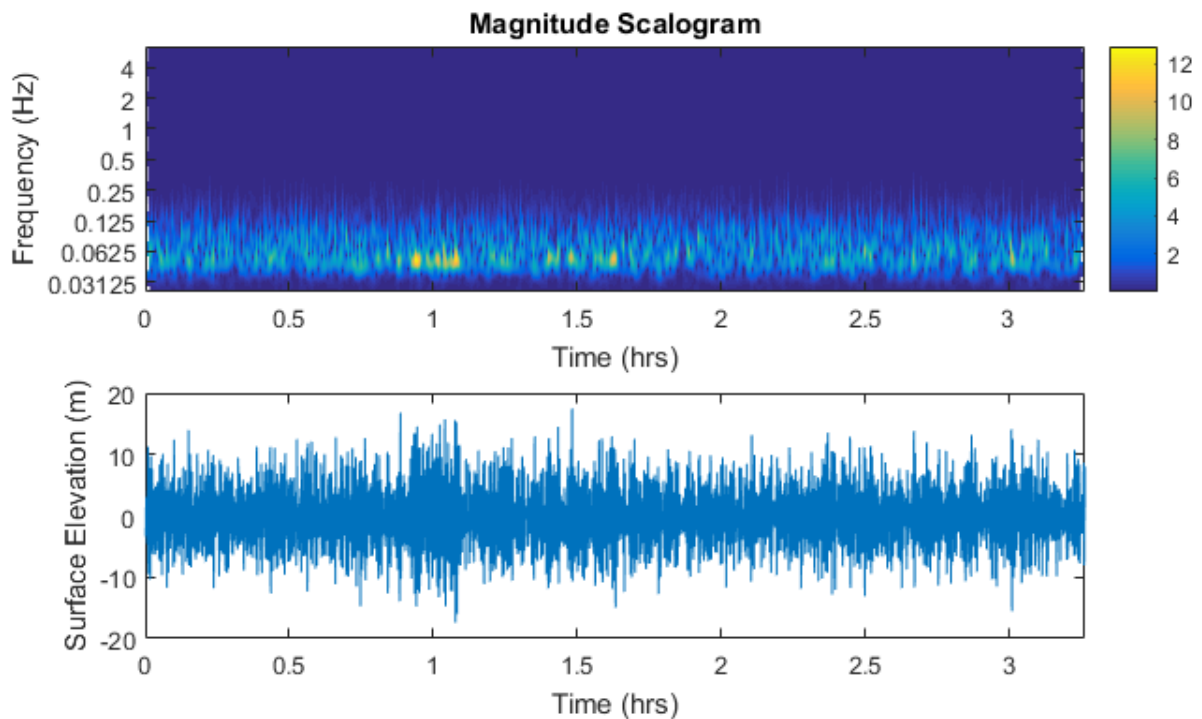

Figure 4-14: Wavelet transform magnitude relative to surface elevation time series

From the wavelet coefficients, the average frequency is calculated for every time instant. The average frequency is computed by the square root of the second spectral moment divided by the zeroth spectral moment, within specified frequency range. Figure 4-15 depicts how the zeroth moment is equivalent to the Riemann sum of the frequency spectrum, and the second

47

moment is the Riemann sum multiplied with the moment arm squared. The area confined by the peak frequency, cut-off frequency and the frequency spectrum are discretized into columns. The lowermost image shows where the resulting average frequency is localized in the frequency spectrum.
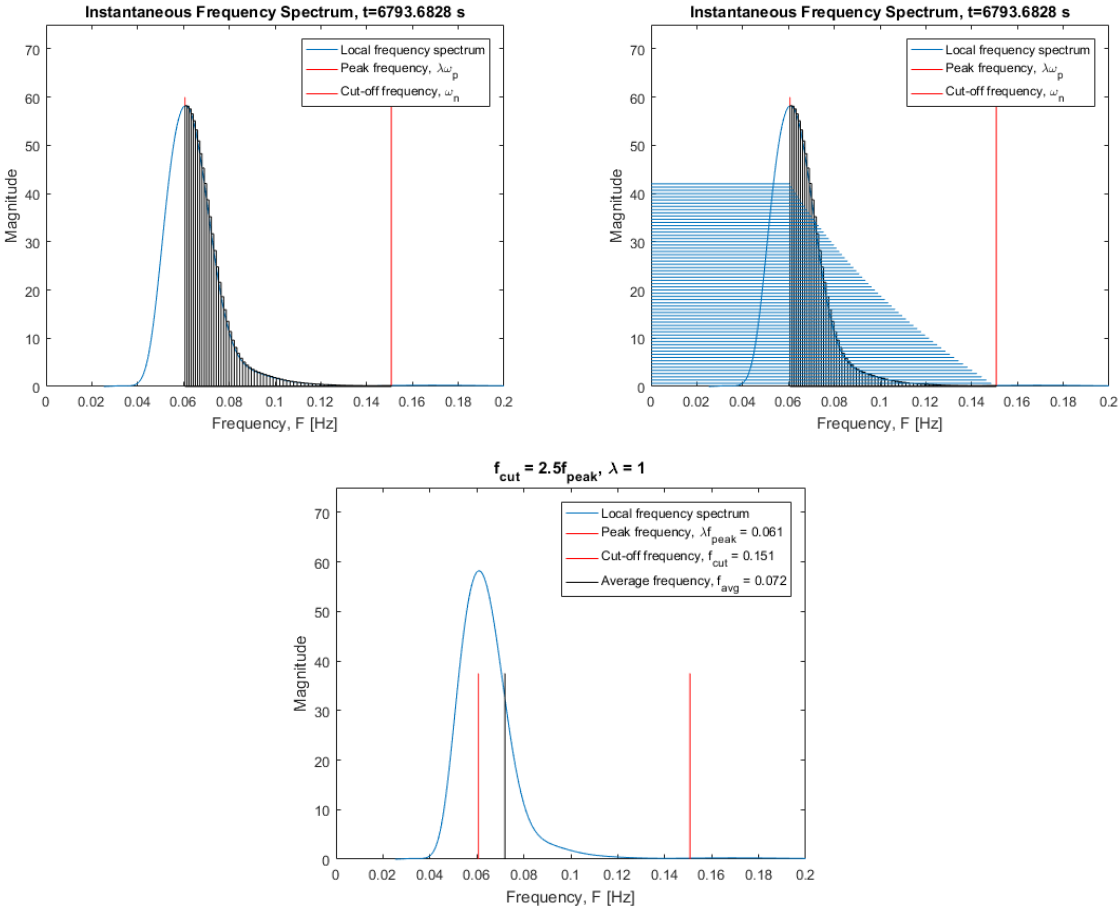
Figure 4-15: Calculation of average frequency

The series of graphs on Figure 4-16 illustrate the last transformation of the surface elevation data. By using the Hilbert-transform the analytical envelope of the surface elevation is computed. The local phase is obtained by computing the angle between the real and complex component of the wavelet coefficients. From the analytical envelope and local phase, the local characteristic amplitude is finally calculated.
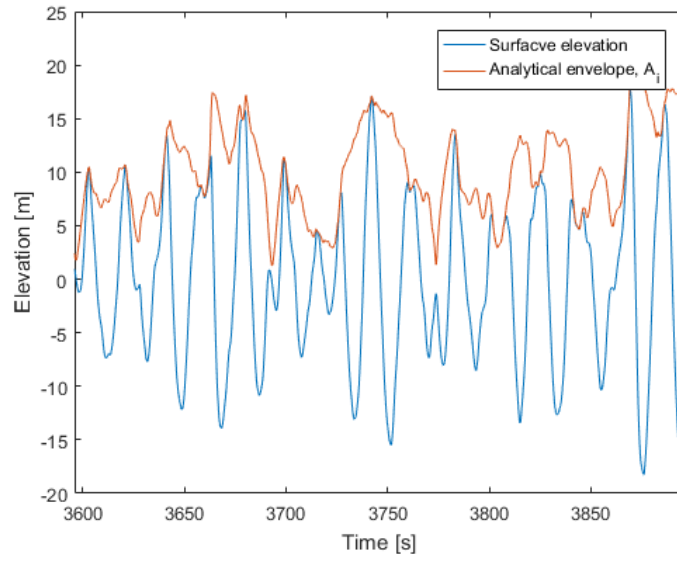
48
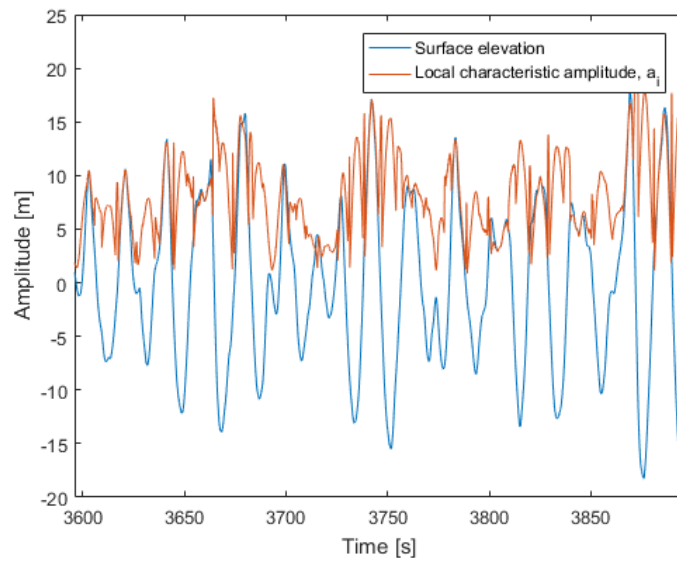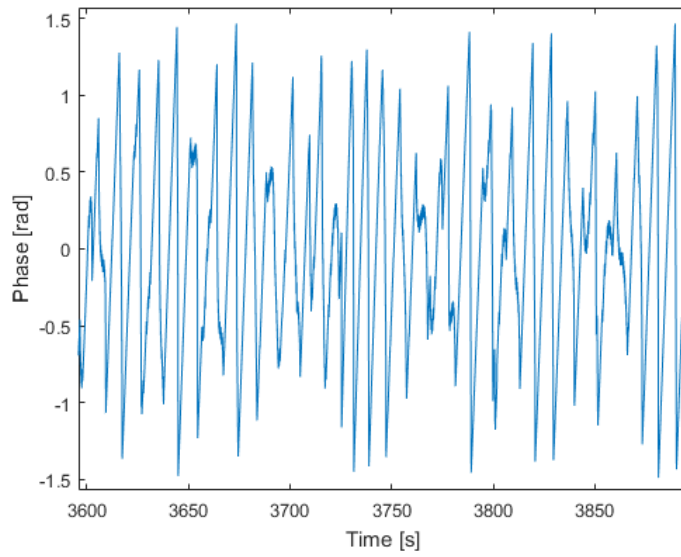
Figure 4-16: Surface envelope, average phase and local characteristic amplitude

Figure 4-17 visualizes the components of the dynamic criterion, more specifically the local amplitude and the local angular frequency squared. The bottom figure is the plot of the resulting acceleration with the threshold value as the orange bar. Wave events with accelerations exceeding the bar are the wave events suspected to break after this method.
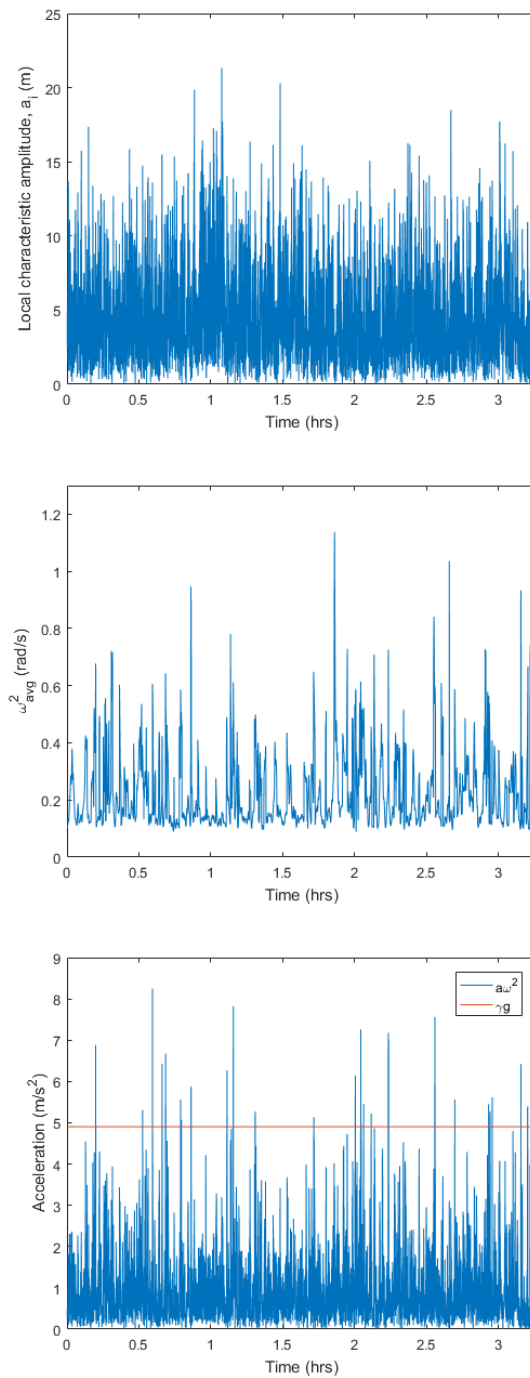

Figure 4-17: The dynamic criterion

For the three selected parameters, the dynamic criterion by the wavelet approach yields 31 wave events suspected to break. From visual inspection of the surface elevation, 19 of them are considered to actual break. Figure 4-18 shows wave events exceeding the limiting acceleration. The title gives the calculated acceleration value and number of wave. The first two rows depict wave events considered to break, while the two events in the second row are deemed as non-breaking events.
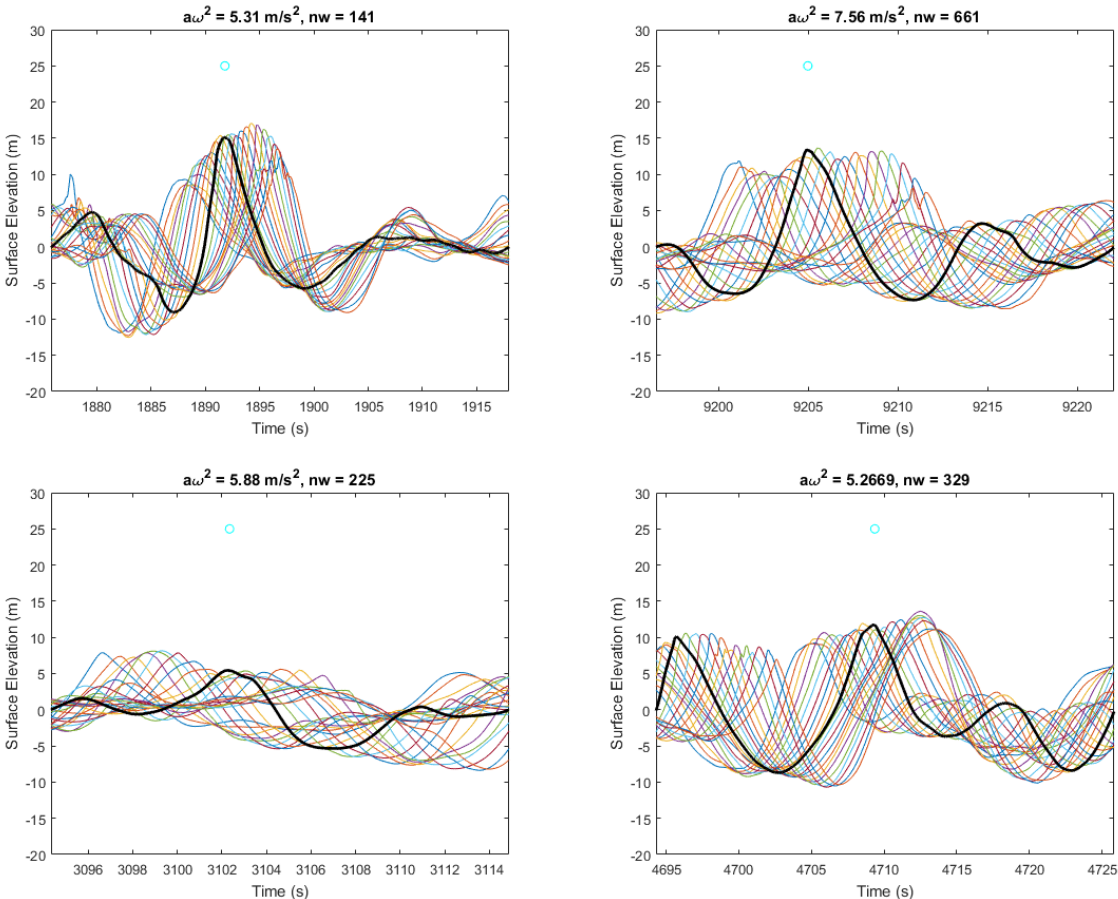

Figure 4-18: Breaking and non-breaking events by the dynamic criterion by CWT

Figure 4-19 shows where the suspected wave breaking events occur marked by cyan circles. The wave events considered to be actual breakers by visual confirmation are marked by black crosses. The performance of this method is summed by the following metrics:

$$DR = 61.3\,\%$$
$$ROFP = 38.7\,\%$$
$$P = 2.24\%$$

51

Which is more accurate than using the geometric criterion, but still not very satisfactory. The occurrence of actual wave breaking events and all detected waves are shown in Figure 4-19. The cyan circles mark all detected waves satisfying the criterion and black crosses are marking which of all detected waves are considered actual wave breaking events.
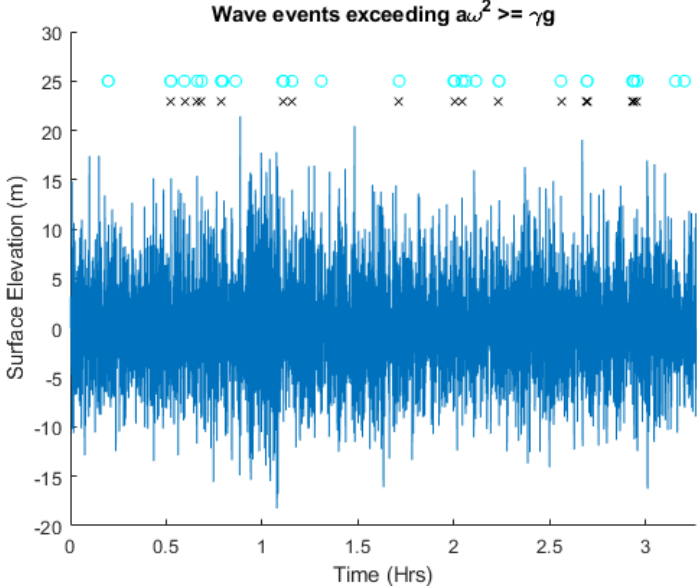

Figure 4-19: Surface elevation and breaking events after dynamic criterion by CWT

This method is not vey easy to implement and a different set of parameters constraining the process yields different performance. However, with a detection rate of 61.3 %, this method is able to find breaking wave events. The rate of false positive could be even lower when the optimal set of parameters are chosen. In addition, the performance may be further improved by making sure of in the calculation process that all detected waves fulfill the dynamic criterion (by Eq. 2-22) at the time of the crest height. All in all, by this method, with the selected parameters and threshold, this method finds that 2.24 % of the wave events are breaking for the first realization. Alternatively, one could also investigate the number of breaking events by calculating the amplitude after Eq. 2-26, and then vary the constraining parameters.

4.5   Wavelet Analysis: Local Energy Density

At first, the power density spectrum is determined as in the methodology. The total local energy density is found by integrating over frequency for all time instants. Figure 4-20 shows the local energy density for every time instant (upper left), how the energy densities form for a smaller time span (upper right), and that the local energy density peaks occur at the crests of the surface elevation (lower). In the bottom image the surface elevation is in blue and is reduced by a factor of 2.5 and the local energy density is graph orange and in original scale.
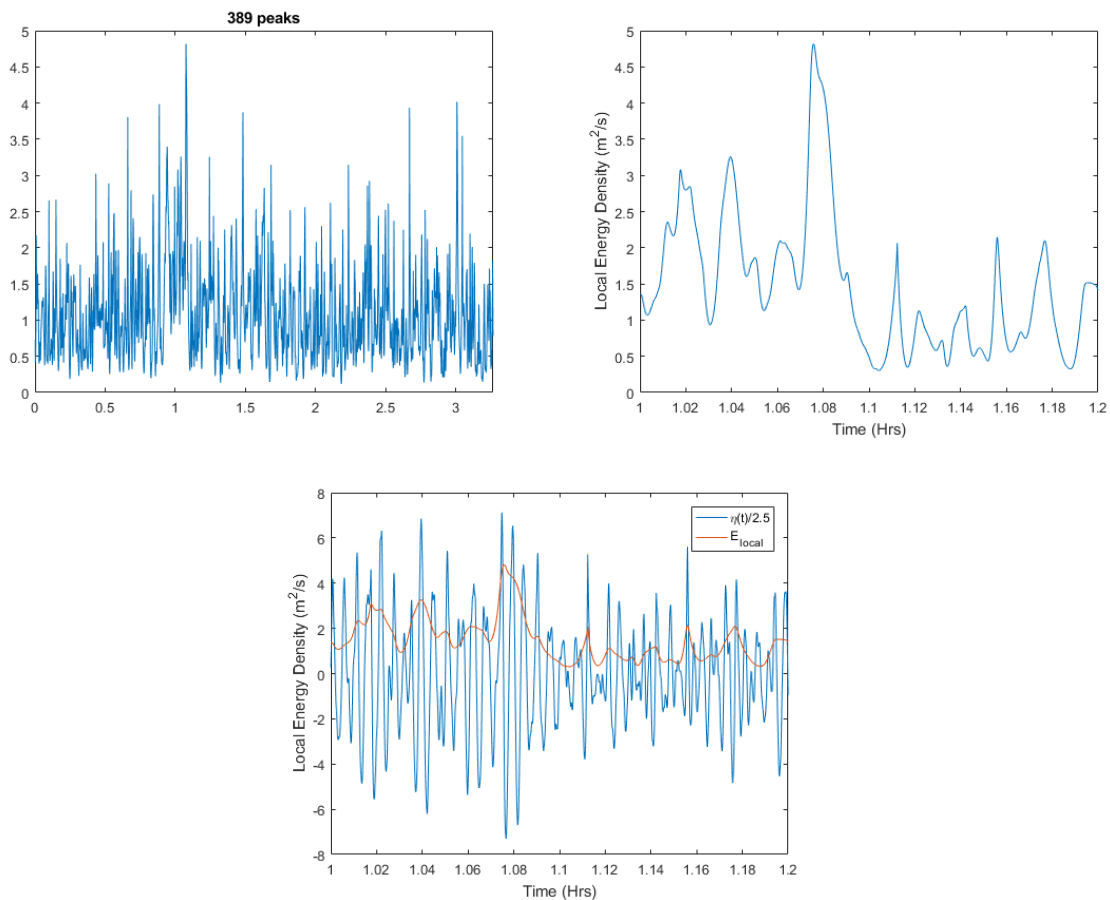

Figure 4-20: Local energy density

Using the *findpeaks*-function, 389 distinct peaks are recognized. That means that there is a little less than one energy density peak per two wave events. The highest local energy density is found to be $E_{local,max} = 4.82\ m^2/s$. Based on this maximum value, a relative limiting threshold value is determined to discriminate non-breaking events. The results from a quick inspection of the number of detected waves when varying this threshold is seen in Table 8:

Table 8: Number of suspected breaking events when varying threshold value

γ	0.5	0.6	0.7
Detected waves	39	17	1

The threshold is therefore selected to be $\gamma = 0.6$ as it yields a reasonable number of waves suspected to breaking. Liberzon and Itay (2017) have a similar approach where they study a so-called coefficient of performance (CP) as a function of a limiting threshold times the maximal energy found in the analysis. The energy of wave events is calculated by a wavelet transform, but with matching the mother wavelet with the instantaneous frequency at the wave crests rather than finding the local energy density at every time instant. However, they find that for different sets of experimental data that the highest CP is found when the limiting energy threshold is 0.6 times the maximal energy.

An example of the computed local energy densities is represented in Figure 4-21. The spectra correspond to two slices in Figure 4-13 at the given time instants in the title of the plot below. The local energy density, E_{local}, is then taken as the area under the graph and their values are given in the title of the plot. A wave event with a peak energy density given in the left image in the figure below, is not suspected to break having that $\gamma E_{local,max} = 2.89\ m^2/s$. The spectrum in the right image has the highest energy density of all peak energy densities.
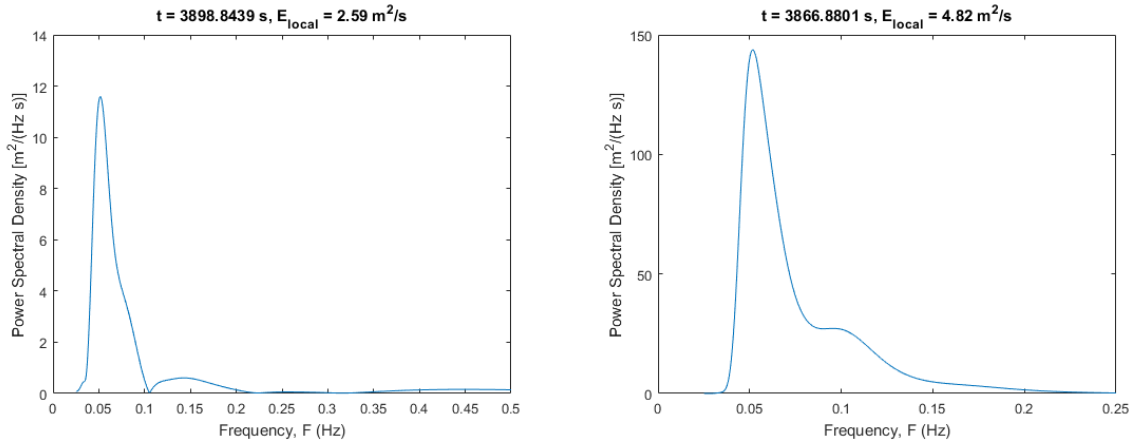

Figure 4-21: Local power spectral density

All local energy densities exceeding the limiting energy threshold are depicted in the upper image of Figure 4-23. In terms of number of waves, 17 wave events are suspected to break according to this limiting energy criterion. Out of these 17 wave events, only two are considered non-breaking, both of which are shown the second row in Figure 4-22. Reading off

from the vertical axes from the plots, it is observed these non-breakers are consider very tall waves. They are a little lower than the significant wave height which is approximately 20.5 meters after scaling. However, since they do not show a decaying trend nor being very sharp at the crest, these waves are not considered to be breaking wave events.
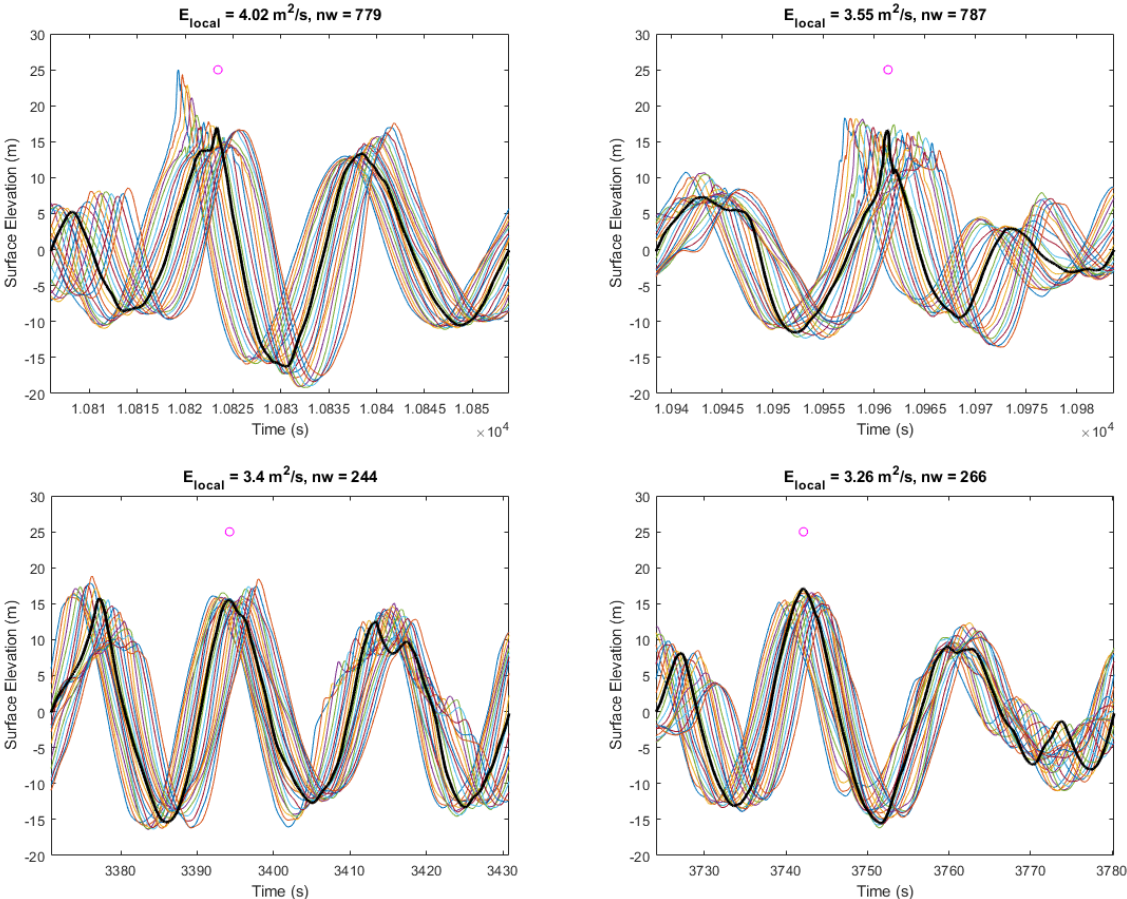

Figure 4-22: Breaking and non-breaking events by the local energy density criterion

The top plot of Figure 4-23 displays the local energy density plot of the continuous wavelet transform against a relative threshold value. Spikes exceeding the threshold value localize in time where the detected breaking events. The bottom plot marks these spikes as circles in magenta where confirmed breaking events are marked as crosses. Consequently, this criterion has the resulting performance:

$$DR = 88.2\ \%$$
$$ROFP = 11.8\ \%$$
$$P = 1.77\ \%$$

55

With a detection rate of 88.2 %, this method proves to be accurate and is much simpler to effectuate than the dynamic criterion by the wavelet approach. The detected waves demonstrate also clear characteristics of breaking. The rate of false positives could be lower if this process becomes more refined. This method is biased to detect the tallest waves, and if the energy or the threshold is defined differently, the performance may increase. The local energy density could be discretized by wave events and the energy density could be represented as a bar diagram. In this way, one could easily compare the energy densities of wave events and inspect whether the wave events with the highest energy densities correlate with breaking events. With $P = 1.77$ %, the applied method also detects few wave events. The threshold may be redefined to admit more wave events. Instead of being relative to the maximal energy density, one could, e.g., find the average of the 20 % of the highest energy densities peaks.
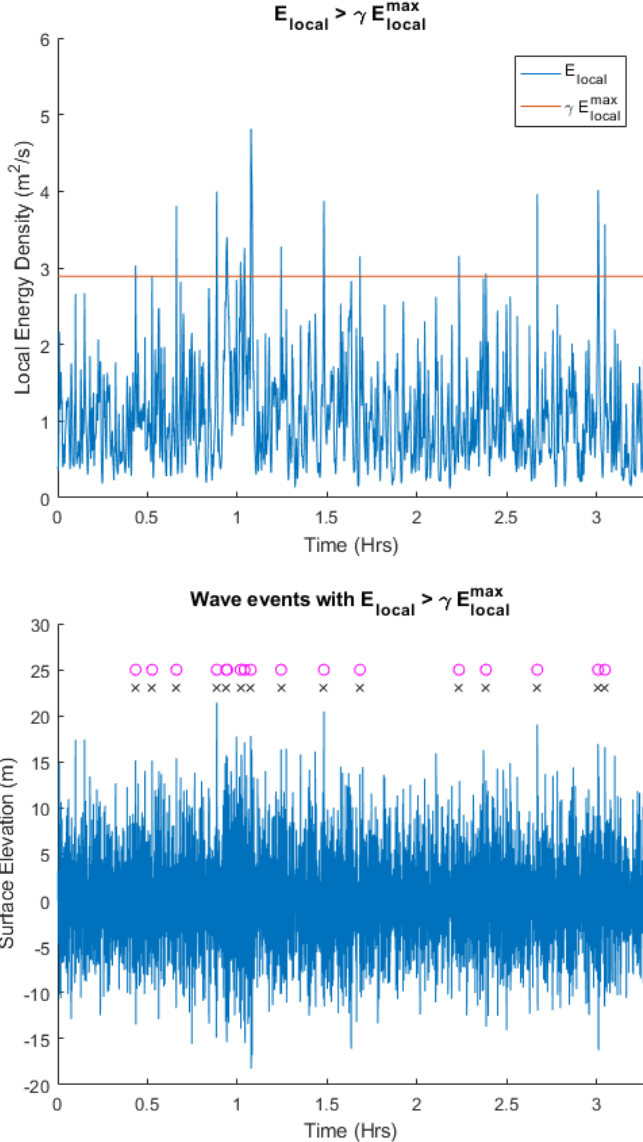

Figure 4-23: Local energy densities exceeding the threshold value

56

4.6   Estimation of Wave Breaking Frequency

All breaking events for all seed numbers are displayed in the series of graphs in Figure 4-24. The circles correspond to the confirmed breaking events that was previously marked as crosses in the previous plots in this chapter. The crosses in Figure 4-24 are compiled by all confir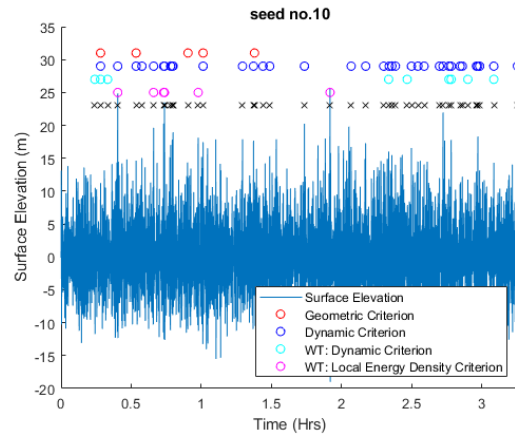med breaking events from the different criteria from the circles above. Thus, this series of plots show strictly breaking events. The coloring scheme is consistent with the previous plots.
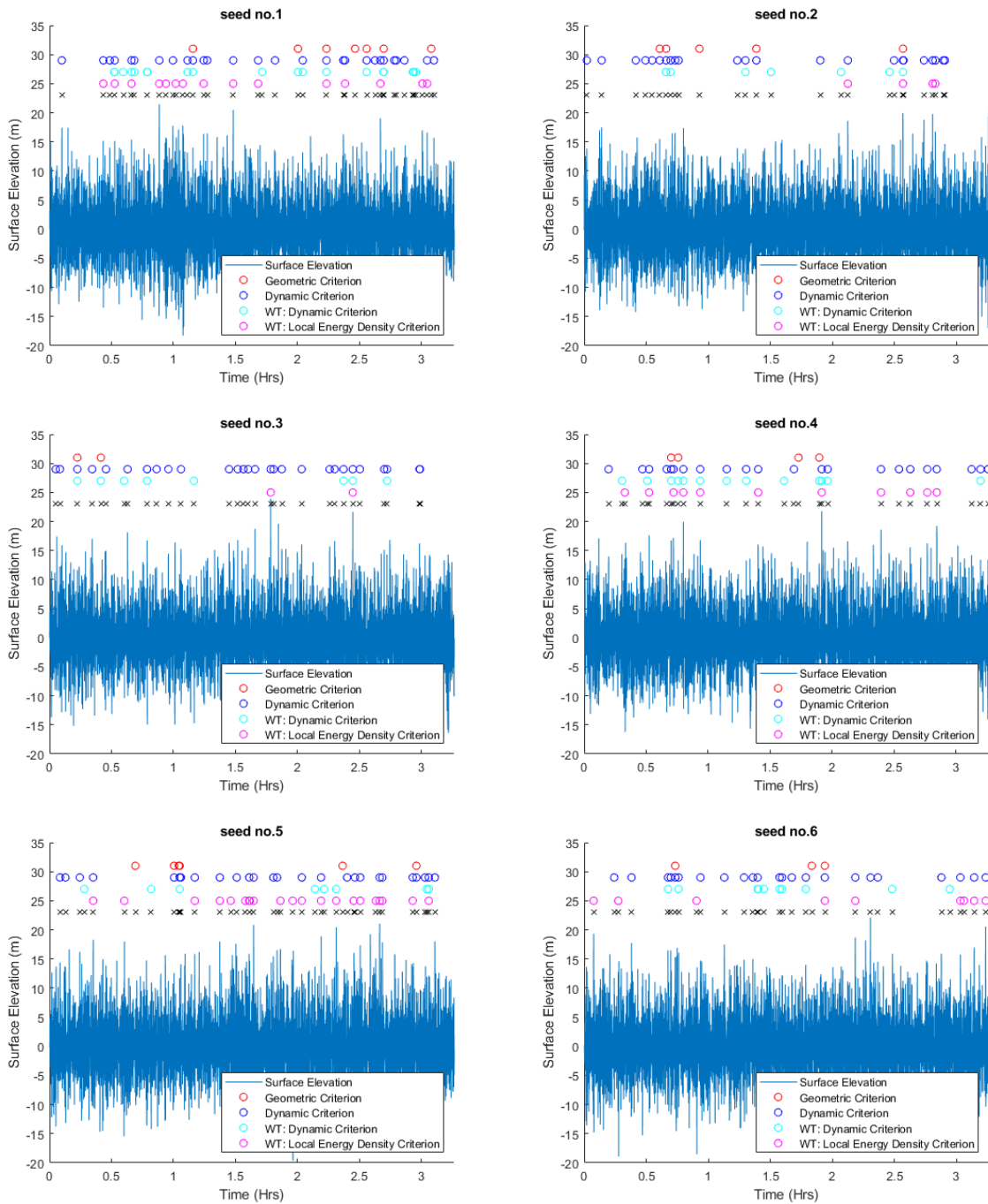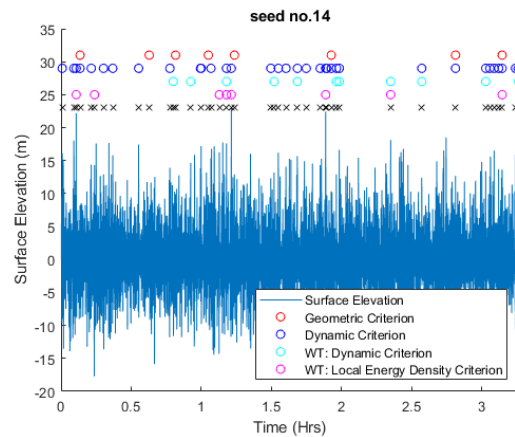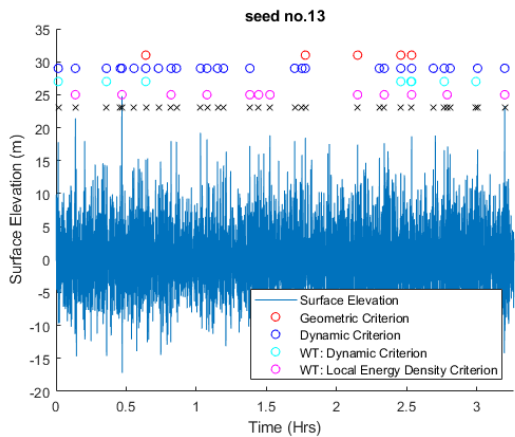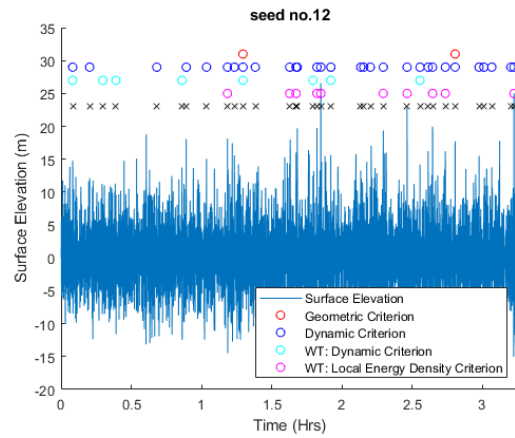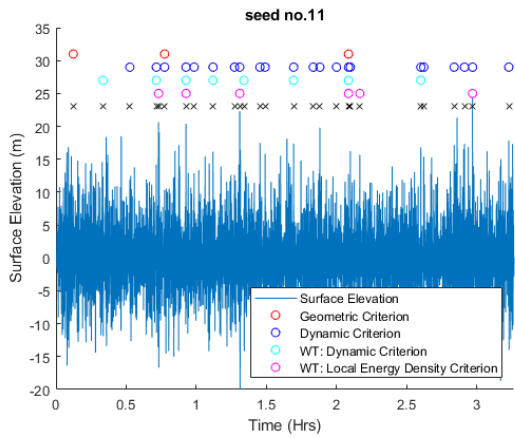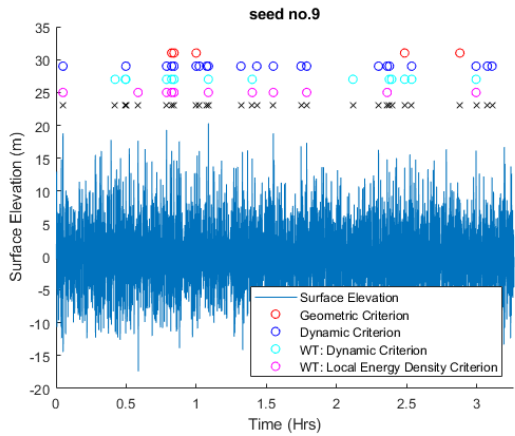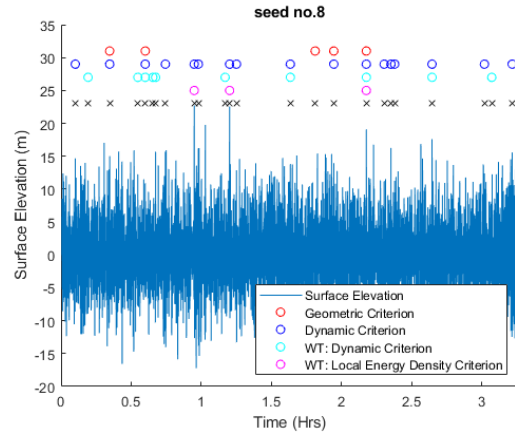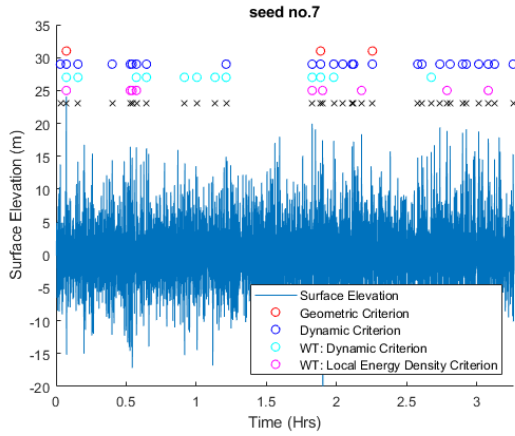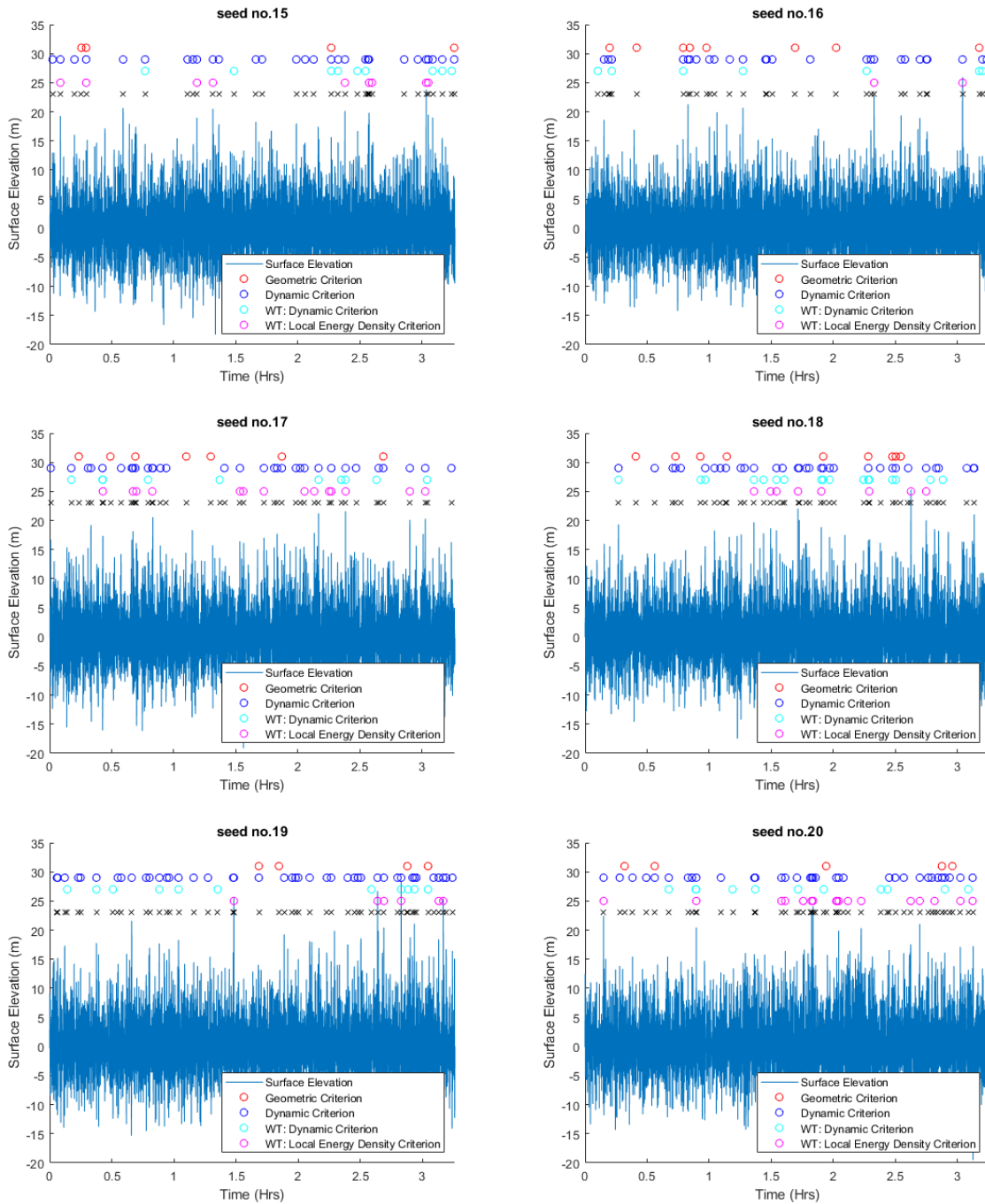
Figure 4-24: Breaking events for all seed numbers

One can immediately register that these plots are dominated by dynamic criterion which finds the most breaking events. From the plots, it is hard to tell whether there exists some underlying patters, e.g. having a high coincidence for the dynamic criteria as they are both in principle measuring the acceleration at the wave crest, or that the criteria that apply the wavelet transform yield similar results. Also, from these plots, it is hard to determine whether the criteria share breaking events as this plot is very narrow and it is not feasible to distinguish neighboring wave events that break.

Figure 4-25, as well as Table 9 and Table 10, give an overview of the performance of the different breaking criteria over all the seed numbers. They illustrate that the results are fairly consistent. They show that geometric criterion has the average highest ROFP with 76.6 %, then dynamic criterion by the wavelet approach with 61.2 %, then two final criteria, namely the dynamic and the local energy density criteria with respectively 10.2 % and 10.3 %. The average breaking frequencies are found to be 0.602 % for geometric criterion, 3.38 % for dynamic criterion, 1.27 % for dynamic criterion by wavelet approach and 1.1 % for the limiting local energy density criterion.
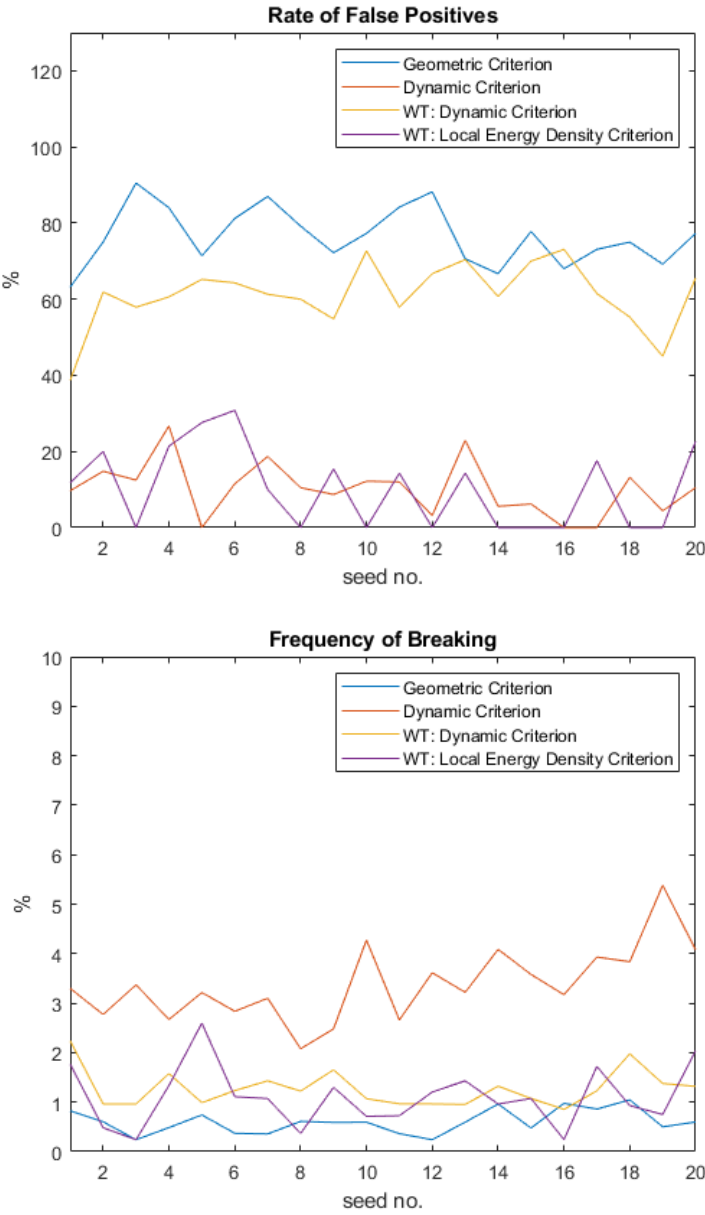
Figure 4-25: Performance of wave breaking criteria

Table 9: Simple statistical properties of the rate of false positives, ROFP (%)

	Geometric	**Dynamic**	**WT: Dynamic**	**WT: LED**
AVG	76.6	10.2	61.2	10.3
STD	7.56	7.20	8.52	10.7

Table 10: Simple statistical properties of breaking frequency, P (%)

	Geometric	**Dynamic**	**WT: Dynamic**	**WT: LED**
AVG	0.602	3.38	1.27	1.10
STD	0.238	0.753	0.365	0.608

To clarify, the standard deviations in the tables above are not given as a percentage relative to the mean of the rate of false positives. The simply describe the standard deviations of the means, where the means are given in percentage. Consequently, the standard deviations have the dimension of a percentage as well.

With the lowest rate of false positives and highest frequency of breaking, it seems like the dynamic criterion without using the wavelet transform is the triumphant method of breaking wave detection.

5   Conclusion and further work

The breaking of waves is a surface process that remains to be fully understood. The last 50 years, a great effort in research has been made to further advance the knowledge on this topic. Traditionally, the indicators of wave breaking have been categorized into three criteria: the geometric criteria, the kinematic criteria and the dynamic criteria. More recent research applies other methods, such as wavelet analysis and growth rate of wave energy, in order to find good indicators of wave breaking as well as to understand why breaking occurs. This study investigates wave breaking with respect to the geometric criterion, two dynamic criterions and a limiting local energy density. The objective of this thesis is trying to determine the frequency of breaking waves.

The geometric criterion, applied to these sets of data, has an average rate of false positives of 76.6 %. It consistently detects non-breaking waves more than actual breaking waves. This criterion also has the lowest average frequency of breaking waves which is calculated to be 0.6 % of all wave events. A reason for this low performance may be due to the assumption of linear relationship of the wave properties, or that the steepness does not capture some underlying nature of breaking events, especially for highly irregular waves.

The dynamic criterion is found to be the most accurate and effective breaking criterion. With an average ROFP of 10 % and breaking frequency of 3.38 %, this criterion performs the best among the investigated criteria. However, one must ask to what extent this criterion, by this calculation method, reflect the dynamical properties of the wave. As this metric really measures the irregularity of the surface shape, this can be more thought of a geometric criterion. It is also believed that the limiting threshold set in this method does not really discriminate accelerations under the threshold value due to the filtration scheme of the data. The true downward accelerations of the confirmed wave events remain unidentified.

The same criterion, but with the wavelet approach different yielded lower results: an average rate of false positives of 61.2 % and an average breaking frequency of 1.27. This method is not very easy to implement and there are several unconstrained parameters that affects the performance. The overall performance may be improved when optimizing this set of parameters.

A simpler and more accurate method by the wavelet approach is carried out. This is done by finding the local energy density spectrum of the continuous wavelet transform. This method yields an average rate of false positives of 10.3 % which is considered a low rate. With an average estimated breaking wave frequency of 1.1%, it is believed there are room for

improvement. The threshold may be redefined to admit more wave events. Instead of being relative to the maximal energy density, one could inspect for an average local energy density of a certain percentage of the highest energy densities. For instance, one can compute the average of the 20 % highest local energy density peaks and combine that value with limiting threshold value.

6 List of references

Babanin, A. V. (2001). Breaking Probabilities for Dominant Surface Waves on Water of Finite Constant Depth. *Journal of Geophysical Research*.

Babanin, A. V. (2011). *Breaking and Dissipation of Ocean Surface Waves.* Melbourne, Australia: Cambridge University Press.

Babanin, A. V., Chalikov, D., & Young, I. R. . (2009). Breaking of Two-dimensional Waves in Deep Water. *International Conference in Ocean Engineering*, pp. 286-395.

Babanin, A. V., Chalikov, D., Young, I. R, & Savelyev, I. (2007). Predicting the Breaking Onset of Surface Water Waves. *Geophysical Research Letters*.

Babanin, A. V., Young, I. R., & Banner, M. L. (1995). Field and Laboratory Observations of Wind Wave Breaking. *The Second International Conference on the Mediterranean Coastal Environment.*

Banner, M. L., & Peirson, W. L. (2007). Wave breaking onset and strength fortwo-dimensional deep-water wave groups. *Journal of Fluid Mechanics*, pp. 93-115.

Banner, M. L., & Tian, X. (1998). On the determination of the onset of breaking formodulating surface gravity water waves. *Journal of Fluid Mechanics*, pp. 107-137.

Barthelemy, X., Banner, M. L., Peirson, L. W., & Fedele, F. (2018). On a unified breaking onset threshold for gravity waves in deep and intermediate depth water. *Journal of Fluid Mechanics*, pp. 463-488.

Chen, C., & Chu, X. (2017). Two-dimensional Morlet wavelet transform and its application to wave recognition methodology of automatically extracting two-dimensional wave packets from lidar observations in Antarctica. *Journal of Atmospheric and Solar–Terrestrial Physics*, pp. 28-47.

Ding, L., & Farmer, D. (1994). Observations of breaking surface wave statistics. *Journal of Physical Oceanography*.

Donelan, M. A., Longuet-Higgins, M., & Turner, J. (1972). Periodicity in whitecaps. *Nature*, pp. 449-451.

Elsayed, M. A. (2008). Application of Continuous Wavelet Analysis in Distinguishing Breaking and Nonbreaking Waves in the Wind–Wave Time Series. *Journal of Coastal Research*, pp. 273-277.

Elsayed, M. A. (2011). Analyzing Wave Breaking in a Barred Beach Using Wavelet. *Journal of Coastal Conservation*, pp. 639–645.

Farge, M. (1992). Wavelet Transforms and Their Applications to Turbulence. *Annual Review of Fluid Mechanics*, pp. 395-457.

Gemmrich, J. R., & Farmer, D. (1999). Observations of the scale and occurence of breaking surfaces. *Journal of Physical Oceanography*.

Holthuijsen, L. H., & Herbers, T. (1986). Statistics of breaking waves observed as whitecaps in the open sea. *Journal of Physical Oceanography*, pp. 290-297.

Irisov, V., & Voronovich, A. (2010). Numerical Simulation of Wave Breaking. *Journal of Physical Oceanography*, pp. 346-364.

Jessup, A. T., Zappa, C., & Yeh, H. (1997). Defining and quantifying microscale wave breaking with infrared imagery. *Journal of Geophysical Research*.

Jinshan, X., Jiwei, T., & Enbo, W. (1998). The Application of Wavelet Transform to Wave Breaking. *Acta Mecanica Sinica*, pp. 306-318.

Kjeldsen, S. P., & Myrhaug, D. (1980). Wave-wave interactions, current-wave interactions and resulting extreme waves and breaking waves. *Proceedings of the 17th Conference on Coastal Engineering.*

Komen, G. L., Cavaleri, L., & Donelan, M. (1994). Dynamics and Modelling of Ocean Waves. *Cambridge University Press*, p. 554.

Lilly, J. M. (2019). *The Wavelet Transform*. Retrieved from jLab: A data analysis package for Matlab: http://www.jmlilly.net/index.html

Liu, P. (1993). Estimating Breaking Wave Statistics from Wind-Wave Time Series Data. *Annales Geophysicae*, pp. 970-972.

Liu, P. C. (1994). Wavelet Spectrum Analysis and Ocean Wind Waves. *Wavelets in Geophysics*, pp. 151-166.

Liu, P. C., & Babanin, A. V. (2004). Using wavelet spectrum analysis to resolve breakingevents in the wind wave time series. *Annales Geophysicae, European Geosciences Union*, pp. 3335-3345.

Longuet-Higgins, M. S. (1969). On wave breaking and equilibrium spectrum of wind. *Proceedings of the Royal Society of London*, pp. 151-159.

Longuet-Higgins, M. S. (1985). Accelerations in steep gravity waves. *Journal of Physical Oceanography*, pp. 1570-1579.

Longuet-Higgins, M. S., & Smith, N. (1983). Measurements of breaking by a surface jump meter. *Journal of Geophysical Research*.

Lowen, M. R., & Melville, W. K. (1991). A model of the sound generated by breaking waves. *The Journal of the Acoustical Society of America*.

Massel, S. R. (2001). Wavelet Analysis for Processing of Ocean Surface Wave Records. *Ocean Engineering*, pp. 957-987.

Massel, S. R. (2007). *Ocean Waves Breaking and Marine Aerosol Fluxes.* Springer.

Mitchell, J. H. (1893). The highest waves in water. *Philosophical Magazine*, pp. 430-437.

Ochi, M. K., & Tsai, C.-H. (1983). Prediction of Occurrence og Breaking Waves in Deep Water. *American Meteorological Society*, pp. 2008-2019.

Philips, O. M. (1958). The equilibrium range in the spectrum of wind-generated waves. *Journal of Fluid Mechanics*, pp. 426-434.

Ramberg, S. E., & Griffin, O. (1987). Laboratory study of steep and breaking deep water waves. *Journal of Waterway, Port and Coastal Ocean Engineering*, pp. 493-507.

Rapp, R. J., & Melville, W. (n.d.). Laboratory measurements of deep water breaking waves. *Philosophical Transactions of the Royal Society of London / A*, pp. 331:735-80.

Rice, S. O. (1954). *Mathematical analysis of random noise. In Noise and Stochastic Processes.* New York: Dover.

Saket, A., Pierson, W. L., Banner, M. L., Barthelemy, X., & Allis, M. J. (2015). Wave breaking onset of two-dimensional deep-water wave groups in the presence and absence of wind. *Unpublished*.

Seiffert, B. R., Ducrozet, G., & Bonnefoy, F. (2017). Simulation ofbreaking waves using the High-Order Spectral method with laboratory experiments: Wave-breakingonset. *Ocean Modelling*.

Smith, M. J., Poulter, E., & McGregor, J. (1996). Doppler radar measurement of wave groups and breaking waves. *Journal of Geophysical Research*.

Snyder, R. L., Smith, L., & Kennedy, R. (1983). On the formation of whitecaps by a threshold mechanism. Part III: Field experiment and comparison with theory. *Journal of Physical Oceanography*, pp. 1505-1518.

Song, J.-B., & Banner, M. L. (2002). On Determining the Onset and Strength of Breaking for Deep Water Waves.Part I: Unforced Irrotational Wave Groups. *American Meteorological Society*, pp. 2541-2558.

Srokosz, M. A. (1985). On the Probability of Breaking Waves in Deep Water. *Journal of Physical Oceanography*, pp. 382-385.

Stansell, P., & MacFarlane, C. (2002). Experimental Investigation of Wave Breaking Criteria Based on Wave Phase Speeds. *American Meteorological Society*, pp. 1269-1283.

Stokes, G. G. (1880). Appendices and supplement to a paper on the theory of oscillatory waves. *Mathematical and Physical Papers. Vol 1*, pp. 219-229.

Têgowski, J. (2004). A lab study on breaking waves. *Oceanologia*, pp. 365-382.

Toffoli, A., Babanin, A. V., Onorato, M., & Waseda, T. (2010). Maximum steepness of oceanic waves: Field and laboratoryexperiments. *Geophysical Research Letters*.

Torrence, C., & Compo, G. P. (1998). A Practical Guide toWavelet Analysis. *Bulletin of the American Meteorological Society*, pp. 61-78.

Wu, C. H., & Nepf, H. M. (2002). Breaking criteria and energy losses for three-dimensional wavebreaking. *Journal of Geophysical Research*.

Zimmerman, C.-A., & Seymour, R. (2002, April). Detection of Breaking in a Deep Water Wave Record. *JOURNAL OF WATERWAY, PORT, COASTAL AND OCEAN ENGINEERING*, pp. 72-78.